An Evaluation of the FCT Method for High-Speed Flows on Structured Overlapping Grids

J.W. Banks [1,2], and W.D. Henshaw [1]

Center for Applied Scientific Computing, Lawrence Livermore National Laboratory,
Livermore, California , 94550

J.N. Shadid [2],

Computational Sciences R&D Group, Sandia National Laboratories,
Albuquerque, New Mexico, 87185-0316

Abstract

This study considers the development and assessment of a Flux-Corrected Transport (FCT) algorithm for simulating high-speed flows on structured overlapping grids. This class of algorithm shows promise for solving some difficult highly-nonlinear problems where robustness and control of certain features, such as maintaining positive densities, is important. Complex, possibly moving, geometry is treated through the use of structured overlapping grids. Adaptive mesh refinement (AMR) is employed to ensure sharp resolution of discontinuities in an efficient manner. Improvements to the FCT algorithm are proposed for the treatment of strong rarefaction waves as well as rarefaction waves containing a sonic point. Simulation results are obtained for a set of test problems and the convergence characteristics are demonstrated and compared to a high-resolution Godunov method. The problems considered are an isolated shock, an isolated contact, a modified Sod shock-tube problem, a two-shock Riemann problem, the Shu-Osher test problem, shock impingement on single cylinder, and irregular Mach reflection of a strong shock striking an inclined plane.

Key words: Euler Equations, Flux Corrected Transport, High Resolution Methods, Overlapping Grids

---

[1] This work was performed under the auspices of the U.S. Department of Energy (DOE) by Lawrence Livermore National Laboratory in part under Contract W-7405-Eng-48 and in part under Contract DE-AC52-07NA27344 and by DOE contracts from the ASCR Applied Math Program.

[2] This work was partially supported by DOE NNSA ASC Algorithms effort and the DOE Office of Science AMR program at Sandia National Laboratory. Sandia is a multiprogram laboratory operated by Sandia Corpo-

1 Introduction

Many physical systems are well described mathematically by systems of conservation laws. Typical examples might include fluid flow around a body, condensed phase explosives, astrophysical phenomenon, or high energy density physics applications. A large number of such systems have the property that discontinuous solutions can arise in finite time even from smooth initial data. These discontinuities can be of a linear (e.g. contact wave) or nonlinear form (e.g. shock wave). Numerical methods need to balance the often competing requirements of accurately approximating these two types of discontinuities while at the same time requiring higher order accuracy in smooth regions of the solution. This balance has been one of the primary drivers behind the development of modern simulation tools. Methods striking such a balance are often referred to as high-resolution methods and they require the use of limiters (switches) that choose between a number of different numerical stencils. For some flow regimes, this type of limiting has been found to be essential to obtain robust schemes. Many, if not most, of the high-resolution techniques have their roots in the 1970's with ideas originally developed by Boris and Book in connection with flux-corrected transport (FCT) [1–3]. In the intervening years, FCT has been applied to a wide range of challenging applications, for examples see [4–6], however the underlying mathematical developments have not been as extensive as for other modern high-resolution techniques such as WENO [7,8], ENO [9–11], and high-resolution Godunov techniques [12–14]. Recently however, the developments of Kuzmin et. al. [6] towards algebraic flux correction as well as implicit methods have produced a renewed interest in FCT as a useful numerical method for many applications.

The scope of our current study is in the evaluation of FCT type methods for compressible flow simulations in the context of overlapping grids which are used to represent geometric complexities as well as ensure mesh regularity [15–18]. The overlapping grid method is quite general and can be used to generate computational meshes for complex geometries [19–21] without the use of unstructured meshes, cut cells for embedded boundaries, or overly contorted globally mapped grids. To our knowledge the FCT method has not been used with this type of infrastructure and one focus of the current study is to evaluate its usefulness in that context. In addition, we present a detailed comparison with a high-resolution Godunov method in order to provide a significant comparison with a more extensively characterized technique.

This paper first examines implementation details for structured overlapping grids. A series of test problems demonstrates the properties of the method for practical simulations and compares the results with those from a high-resolution Godunov method. Reference to the results presented in other studies such as [22,23] gives a good understanding of the relative merits of these various high-resolution shock capturing schemes. This comparison is particularly useful for cases where Riemann solution based strategies are not viable because of the complexities of the governing equations. Such is the case for some relativistic flows, for example, and the FCT method may be attractive in this context provided an appropriate low order method can be devised without resort to Riemann solutions. As shown in [24], FCT can also be useful for problems with extreme jumps in density and pressure where traditional high-resolution methods may fail due to unphysical states such as negative densities. It should be noted that FCT-FEM methods are currently being used to effectively solve difficult problems in complex geometry using unstructured meshes [6]. In this finite element context, there is a need to solve problems with strong shocks and other discontinuities, but there are very few continuous finite element counterparts to high-resolution finite-volume and finite-difference methods. It is thus important to understand the relative merits of FCT and other high-resolution schemes in a framework where a valid comparison can be made.

The remainder of the paper is structured as follows. In Section 2 the governing equations are presented. In Section 3 the FCT algorithm is presented and the development for structured overlapping grids is summarized. This section also presents a brief discussion of two open issues with the traditional FCT algorithm; that of

---

ration, a Lockheed Martin Company, for the United States Department of Energy's National Nuclear Security Administration under contract DEM-AC04-94AL85000.

performance when either strong or sonic rarefactions are present in the flow. The poor performance of the standard method for these problems is demonstrated and an improvement of the algorithm is proposed and evaluated. Section 4 presents numerical results for the FCT method and provides a comparison to a high-resolution Godunov method. Some qualitative remarks concerning computational cost comparisons between the FCT and Godunov methods are presented in Section 5 and concluding remarks are given in Section 6.

2 Governing Equations

In this paper we consider the flow of an inviscid compressible gas and assume that in two dimensions the density ρ, velocities (u_1, u_2), pressure p, and total energy E satisfy the system of conservation laws

$$\frac{\partial}{\partial t}\mathbf{u} + \frac{\partial}{\partial x_1}\mathbf{f}_1(\mathbf{u}) + \frac{\partial}{\partial x_2}\mathbf{f}_2(\mathbf{u}) = 0, \tag{1}$$

where

$$\mathbf{u} = \begin{bmatrix} \rho \\ \rho u_1 \\ \rho u_2 \\ E \end{bmatrix} \qquad \mathbf{f}_1(\mathbf{u}) = \begin{bmatrix} \rho u_1 \\ \rho {u_1}^2 + p \\ \rho u_1 u_2 \\ u_1(E+p) \end{bmatrix} \qquad \mathbf{f}_2(\mathbf{u}) = \begin{bmatrix} \rho u_2 \\ \rho u_1 u_2 \\ \rho {u_2}^2 + p \\ u_2(E+p) \end{bmatrix}.$$

System (1) defines the conservation of mass, momenta, and total energy for the gas and is recognized as the well known compressible Euler equations in two space dimensions. In this formulation, the total energy is given by

$$E = \rho e + \frac{1}{2}\rho\left({u_1}^2 + {u_2}^2\right),$$

where $e = e(\rho, p)$ is the specific internal energy, which is specified by an equation of state. This paper assumes an ideal equation of state, namely

$$e = \frac{p}{\rho\,(\gamma - 1)} \tag{2}$$

where $\gamma = \frac{c_p}{c_v}$ is the ratio of (constant) specific heats with c_p the specific heat at constant pressure and c_v the specific heat at constant volume. The Euler equations (1) are assumed to have been non-dimensionalized with suitable reference quantities and all results are presented in dimensionless units.

3 Flux-Corrected-Transport Algorithm

This section describes the FCT method as used in this paper including the extensions and modifications we have made to the classic FCT algorithm. This implementation includes a DeVore type pre-limiter in lieu of Zalesak's flux pre-constraint, removal of artificial diffusion prior to the FCT flux limiter, a Jameson style artificial viscosity, a sonic fix for entropy violating rarefaction waves, and the extension of the FCT algorithm to overlapping grids. For clarity, the improvements for treating sonic points and very strong rarefactions are left to the end of the section.

3.1 Overlapping grids and AMR

We consider the governing equations (1) and proceed with a description of the FCT method in a two dimensional overlapping grid framework. To this end, we assume the flow domain is given by Ω and is discretized using an overlapping grid $\mathcal{G}$. The overlapping grid consists of a set of component grids $\{\mathcal{G}_i\}$, $i = 1, \ldots, \mathcal{N}_g$, that cover Ω and overlap where they meet. Each component grid covers a sub-domain Ω_i. Grid points are tagged as discretization points where the governing equations are applied, ghost points used for the application of boundary conditions, interpolation points where solution values are communicated between grids, or unused points where no computation is performed which are cut out through the mesh generation procedure. The FCT stencil is 7-points wide requiring three layers of data at interpolation and physical boundaries. At interpolation boundaries, the 7-point stencil would normally require three layers of interpolation points. Although we can generate such grids, in practice we usually construct a grid with a single layer of interpolation points and obtain values at the two additional layers through extrapolation. At physical boundaries, values on the boundary and three layers of ghost points are obtained through application of the physical boundary conditions, derived compatibility conditions, and extrapolation following the approach described in [16,17]. Note that the dependence of the solution on this final extrapolated layer is extremely weak as it can only affect whether the chosen update at the boundary is first or second order accurate (i.e. it is used only in the determination of the $\boldsymbol{\alpha}$ in (8) below. For more details concerning general overlapping grid methods, including application of boundary conditions, see [15–17,25]. Adaptive mesh refinement (AMR) is used in regions of the flow where the solution changes rapidly, such as near shocks and contact surfaces. We employ a block-structured AMR approach following that described originally in [26] and using modifications for overlapping grids as presented in [16–18].

3.2 FCT Discretization on a mapped grid

Each component grid, including base-level grids and any refined grids, is defined by a mapping from the unit square in computational space (r_1, r_2) to physical space (x_1, x_2). In computational space, equation (1) becomes

$$\frac{\partial}{\partial t}\mathbf{u} + \frac{1}{J}\frac{\partial}{\partial r_1}\mathbf{F}_1(\mathbf{u}) + \frac{1}{J}\frac{\partial}{\partial r_2}\mathbf{F}_2(\mathbf{u}) = 0, \tag{3}$$

where

$$\mathbf{F}_1(\mathbf{u}) = J\left(\frac{\partial r_1}{\partial x_1}\mathbf{f}_1 + \frac{\partial r_1}{\partial x_2}\mathbf{f}_2\right), \qquad \mathbf{F}_2(\mathbf{u}) = J\left(\frac{\partial r_2}{\partial x_1}\mathbf{f}_1 + \frac{\partial r_2}{\partial x_2}\mathbf{f}_2\right),$$

and

$$J = \left|\frac{\partial(x_1, x_2)}{\partial(r_1, r_2)}\right|.$$

The metrics of the mapping, $\partial x_1/\partial r_2$, $\partial x_2/\partial r_2$, etc., and the Jacobian are considered to be known for each component grid at the time of computation and can be generated analytically or approximated.

Discretization of (3) is performed using a uniform grid $(r_{1,i}, r_{2,j})$ with grid spacing $(\Delta r_1, \Delta r_2)$. The FCT method is generally considered a two-step process proceeding first with a low order update and finishing with the high-resolution FCT correction. We begin with the formulation of the low order solution update

$$\mathbf{u}_{i,j}^{\text{td},n} = \mathbf{u}_{i,j}^{n} - \frac{\Delta t}{J_{i,j}\Delta r_1} D_{+r_1}\mathbf{F_1}_{i-1/2,j}^{\text{low},n} - \frac{\Delta t}{J_{i,j}\Delta r_2} D_{+r_2}\mathbf{F_2}_{i,j-1/2}^{\text{low},n} \tag{4}$$

where D_{+r_1} and D_{+r_2} are the undivided forward difference approximations in the r_1 and r_2 directions of index space respectively. The "td" notation is consistent with [1–3,27] and denotes "transported and diffused". For this work the HLL low order flux [12,14] is used and for curvilinear geometries is given by

$$\mathbf{F_1}_{i+1/2,j}^{\text{low},n} = \begin{cases} \mathbf{F_1}_{i,j}^{n} & \text{if} \quad s_- \geq 0 \\ \mathbf{F_1}_{i+1,j}^{n} & \text{if} \quad s_+ \leq 0 \\ \dfrac{s_+}{s_+ - s_-}\mathbf{F_1}_{i,j}^{n} - \dfrac{s_-}{s_+ - s_-}\mathbf{F_1}_{i+1,j}^{n} + \dfrac{s_- s_+}{s_+ - s_-} D_{+r_1}\mathbf{u}_{i,j}^{n} & \text{else} \end{cases} \tag{5}$$

where

$$s_- = \min\left(v_{i,j}^n - c_{i,j}^n, v_{i+1,j}^n - c_{i+1,j}^n\right)\left|\left|\left(\frac{\partial r_1}{\partial x_1}, \frac{\partial r_1}{\partial x_2}\right)\right|\right|_2,$$

$$s_+ = \max\left(v_{i,j}^n + c_{i,j}^n, v_{i+1,j}^n + c_{i+1,j}^n\right)\left|\left|\left(\frac{\partial r_1}{\partial x_1}, \frac{\partial r_1}{\partial x_2}\right)\right|\right|_2,$$

$c_{i,j}^n$ is the sound speed in a given cell, and $v_{i,j}^n$ is the component of the velocity normal to the cell face. The fluxes across other cell boundaries take similar forms.

It should be noted that in [28,6], Zalesak suggests the use of the Rusanov flux for the low order method. This is a symmetrized version of the HLL flux resulting in further diffusion than the original HLL flux. However, the Rusanov flux as presented in [28,6] is slightly flawed in that the selected wave speed is not sufficient to encompass the full Riemann solution for all cases. A more general Rusanov flux is

$$\mathbf{F_1}_{i+1/2,j}^{\text{low},n} = \frac{1}{2}\left[\left(\mathbf{F_1}_{i+1,j}^n + \mathbf{F_1}_{i,j}^n\right) - \max\left(\left|\lambda_{i+1,j}^n\right|, \left|\lambda_{i,j}^n\right|\right) D_{+r_1}\mathbf{u}_{i,j}^n\right] \tag{6}$$

where $\lambda_{i,j}^n$ is the largest eigenvalue (in magnitude) of the Jacobian matrix $\frac{\partial}{\partial \mathbf{u}}\mathbf{F}_1$ at a cell (i,j) and time t_n. The difference between (6) and the equation presented in [28,6] is the use of $\max\left(\left|\lambda_{i+1,j}^n\right|, \left|\lambda_{i,j}^n\right|\right)$ rather than $1/2\left(\left|\lambda_{i+1,j}^n\right| + \left|\lambda_{i,j}^n\right|\right)$. In this work, the HLL flux is used but we have found that the Rusanov flux (6) works nearly as well and is less expensive. As presented, both of these approximate fluxes require knowledge of the eigenvalues of the Jacobian matrix. If this information were not known, a Lax-Friedrichs type flux could in principle be used instead.

The second step of the FCT algorithm requires an "anti-diffusive" flux which is defined as the difference between a high-order flux and the low-order one. In the r_1 direction of index space for example, this is

$$\mathbf{F_1}_{i\pm1/2,j}^{\text{AD},n} = \mathbf{F_1}_{i\pm1/2,j}^{\text{high},n} - \mathbf{F_1}_{i\pm1/2,j}^{\text{low},n}. \tag{7}$$

The high order flux is typically chosen to be some high-order centered flux and for this work the centered second-order flux

$$\mathbf{F_1}_{i+1/2,j}^{\text{high},n} = \frac{1}{2}\left(\mathbf{F_1}_{i,j}^n + \mathbf{F_1}_{i+1,j}^n\right)$$

is chosen. The final sub-step update is now defined as

$$\mathbf{u}_{i,j}^{\text{new}} = \mathbf{u}_{i,j}^{\text{td},n} - \frac{\Delta t}{J_{i,j}\Delta r_1}D_{+r_1}\left(\boldsymbol{\alpha}_{i-1/2,j}^n \odot \mathbf{F_1}_{i-1/2,j}^{\text{AD},n}\right) - \frac{\Delta t}{J_{i,j}\Delta r_2}D_{+r_2}\left(\boldsymbol{\alpha}_{i,j-1/2}^n \odot \mathbf{F_2}_{i,j-1/2}^{\text{AD},n}\right) \tag{8}$$

where $\odot$ indicates component-wise multiplication. The vector of $\boldsymbol{\alpha}$'s are chosen using the FCT algorithm as described below and represent the proportion of anti-diffusive flux at each cell face that is used in the final update. Our choice of notation facilitates the use of the FCT algorithm in a method of lines type approach. By defining

$$\frac{\partial}{\partial t}\mathbf{u}_{i,j}^n = \frac{\mathbf{u}_{i,j}^{\text{new}} - \mathbf{u}_{i,j}^n}{\Delta t} \tag{9}$$

we obtain an updated solution $\mathbf{u}_{i,j}^{n+1}$ using any ordinary differential equation (ODE) integrator we choose. Choices for ODE integrators might include Runge-Kutta methods, Adams methods, or others. For this work, we use an explicit Adams predictor-corrector method of second order to match the spatial algorithm. Detail concerning the implementation of these time integrators can be found for example in [29,25].

Consider the determination of $\boldsymbol{\alpha}_{i+1/2,j}^n$. FCT seeks to enforce solution monotonicity through the choice of $\boldsymbol{\alpha}$, but the property of monotonicity is valid only for characteristic variables [30]. For the non-linear Euler equations, conversion to characteristic variables requires both a linearization and an eigen-decomposition of the linearized problem. As such, we linearize about the arithmetic average $\bar{\mathbf{u}} = \frac{1}{2}(\mathbf{u}_{i,j}^{\text{td},n} + \mathbf{u}_{i+1,j}^{\text{td},n})$. More sophisticated choices, such as the Roe average [14], could be made but in our experience these make little difference in the eventual computed solutions. From this state, the linearized eigen-decomposition $\mathbf{T}^{-1}\mathbf{\Lambda}\mathbf{T} = \mathbf{A} = \frac{\partial}{\partial \mathbf{u}}\mathbf{F}_1(\bar{\mathbf{u}})$ is found where we have dropped the sub- and superscripts to simplify the exposition. Whenever multiplication by $\mathbf{T}$ is performed to achieve characteristic quantities it should be understood that this implies linearization about a particular face, in this case $(i+1/2, j)$. For two dimensions, a large number of characteristic transformations must be performed (in three dimensions the number is even larger) and this constitutes one of the most expensive parts of the FCT method.

In [4], DeVore indicates that the scheme of Zalesak does not preserve monotonicity in two dimensions and suggests limiting the fluxes using the original Boris/Book limiter [1,2] in each direction prior to their input to the multi-dimensional limiter. This is straight forward to and we demonstrate it for ${\mathbf{F}_1}^{\mathrm{AD},n}_{i+1/2,j}$

$$\hat{\mathbf{F}}{}_1{}^{\mathrm{AD},n}_{i+1/2,j} = \mathbf{s} \odot \max\left[0, \min\left(\left|\mathbf{T}{\mathbf{F}_1}^{\mathrm{AD},n}_{i+1/2,j}\right|, \mathbf{s} \odot \frac{J_{i+1/2,j}\Delta r_1}{\Delta t} D_{+r_1}\mathbf{T}\mathbf{u}^{\mathrm{td},n}_{i+1/2,j}, \mathbf{s} \odot \frac{J_{i+1/2,j}\Delta r_1}{\Delta t} D_{+r_1}\mathbf{T}\mathbf{u}^{\mathrm{td},n}_{i-1/2,j}\right)\right],$$

where $\mathbf{s} = \mathrm{sign}(\mathbf{T}{\mathbf{F}_1}^{\mathrm{AD},n}_{i+1/2,j})$ and the "hat" notation indicates that the anti-diffusive flux has been pre-limited. The other $\hat{\mathbf{F}}$ fluxes are obtained through similar formulas.

To complete the FCT algorithm, define the local maximum and minimum characteristic values as

$$\begin{aligned}
\mathbf{w}_k^{\max} &= \max\left(\mathbf{T}\mathbf{u}^{\mathrm{td},n}_{i+k-1,j}, \mathbf{T}\mathbf{u}^{\mathrm{td},n}_{i+k,j}, \mathbf{T}\mathbf{u}^{\mathrm{td},n}_{i+k+1,j}, \mathbf{T}\mathbf{u}^{\mathrm{td},n}_{i+k,j-1}, \mathbf{T}\mathbf{u}^{\mathrm{td},n}_{i+k,j+1}\right), \\
\mathbf{w}_k^{\min} &= \min\left(\mathbf{T}\mathbf{u}^{\mathrm{td},n}_{i+k-1,j}, \mathbf{T}\mathbf{u}^{\mathrm{td},n}_{i+k,j}, \mathbf{T}\mathbf{u}^{\mathrm{td},n}_{i+k+1,j}, \mathbf{T}\mathbf{u}^{\mathrm{td},n}_{i+k,j-1}, \mathbf{T}\mathbf{u}^{\mathrm{td},n}_{i+k,j+1}\right),
\end{aligned} \tag{10}$$

where $k = 0, 1$ and the extrema are taken component-wise. The actual influx into the cells on either side of the cell face which would result from the AD fluxes is computed for example as

$$\begin{aligned}
\mathbf{I}_k = \ & \tfrac{1}{\Delta r_1}\left[\max\left(\frac{\hat{\mathbf{F}}{}_1{}^{\mathrm{AD},n}_{i+k-1/2,j}}{J_{i+k,j}}, 0\right) - \min\left(\frac{\hat{\mathbf{F}}{}_1{}^{\mathrm{AD},n}_{i+k+1/2,j}}{J_{i+k,j}}, 0\right)\right] \\
& + \tfrac{1}{\Delta r_2}\left[\max\left(\frac{\hat{\mathbf{F}}{}_2{}^{\mathrm{AD},n}_{i+k,j-1/2}}{J_{i+k,j}}, 0\right) - \min\left(\frac{\hat{\mathbf{F}}{}_2{}^{\mathrm{AD},n}_{i+k,j+1/2}}{J_{i+k,j}}, 0\right)\right],
\end{aligned} \tag{11}$$

and the maximum permissible influx such that the characteristic bounds from (10) are not violated, indicated by the tilde, is for example

$$\tilde{\mathbf{I}}_k = \frac{1}{\Delta t}\left[\mathbf{w}_k^{\max} - \mathbf{T}\mathbf{u}^{\mathrm{td},n}_{i+k,j}\right]. \tag{12}$$

Notice in (11) that the influx into the cells from both direction of index space are considered simultaneously. This follows from [27] and reflects the fully multi-dimensional nature of this limiter as opposed to a limiter which is split along dimensional lines. Component-wise ratios of permissible to actual fluxes are then defined for the two cells as

$$\mathbf{R}_k^+ = \min\left(\frac{\tilde{\mathbf{I}}_k}{\mathbf{I}_k}, 1\right). \tag{13}$$

The quantities $\mathbf{R}_k^-$, which represent the ratio of actual AD flux leaving the cell to the maximum flux permitted to leave the cell without violation of the bounds in (10), are defined using similar reasoning. Setting

$$\begin{aligned}
\mathbf{O}_k = \ & \tfrac{1}{\Delta r_1}\left[\max\left(\frac{\hat{\mathbf{F}}{}_1{}^{\mathrm{AD},n}_{i+k+1/2,j}}{J_{i+k,j}}, 0\right) - \min\left(\frac{\hat{\mathbf{F}}{}_1{}^{\mathrm{AD},n}_{i+k-1/2,j}}{J_{i+k,j}}, 0\right)\right] \\
& + \tfrac{1}{\Delta r_2}\left[\max\left(\frac{\hat{\mathbf{F}}{}_2{}^{\mathrm{AD},n}_{i+k,j+1/2}}{J_{i+k,j}}, 0\right) - \min\left(\frac{\hat{\mathbf{F}}{}_2{}^{\mathrm{AD},n}_{i+k,j-1/2}}{J_{i+k,j}}, 0\right)\right],
\end{aligned} \tag{14}$$

and

$$\tilde{\mathbf{O}}_k = \frac{1}{\Delta t}\left[\mathbf{T}\mathbf{u}^{\text{td},n}_{i+k,j} - \mathbf{w}^{\text{min}}_k\right], \tag{15}$$

we define

$$\mathbf{R}^-_k = \min\left(\frac{\tilde{\mathbf{O}}_k}{\mathbf{O}_k}, 1\right). \tag{16}$$

By choosing the most restrictive of these $\mathbf{R}$ values, the bounds from (10) are not violated. Thus we define

$$\boldsymbol{\beta} = \begin{cases} \min(\mathbf{R}^+_0, \mathbf{R}^-_1) & \text{when} \quad J_{i,j}\hat{\mathbf{F}}{1}^{\text{AD},n}_{i+1/2,j} < 0 \\ \min(\mathbf{R}^+_1, \mathbf{R}^-_0) & \text{when} \quad J_{i,j}\hat{\mathbf{F}}{1}^{\text{AD},n}_{i+1/2,j} \geq 0. \end{cases} \tag{17}$$

The final values for $\boldsymbol{\alpha}^n_{i+1/2,j}$ are found through component-wise inversion of the formula

$$\boldsymbol{\alpha}^n_{i+1/2,j} \odot \mathbf{F}{1}^{\text{AD},n}_{i+1/2,j} = \mathbf{T}^{-1}\Big(\boldsymbol{\beta} \odot \hat{\mathbf{F}}{1}^{\text{AD},n}_{i+1/2,j}\Big). \tag{18}$$

It is important to note that monotonicity of the linearized characteristic variables does not imply monotonicity of the conserved variables. Thus the final updated solution could result in a negative density, imaginary sound speed, or negative pressure. Such events do occur in the simulations we present and must be treated in a rational and reasonable way. Zalesak suggests in [27,6] that a fail-safe limiter be employed and we take a similar approach here. At each time, if the values at a given cell (i, j) violate physically realistic bounds after advancement to $\mathbf{u}^{\text{new}}_{i,j}$ in (8), then no portion of the anti-diffusive flux is allowed at the boundaries of that cell. For such cells,

$$\boldsymbol{\alpha}^n_{i+1/2,j} = \boldsymbol{\alpha}^n_{i-1/2,j} = \boldsymbol{\alpha}^n_{i,j+1/2} = \boldsymbol{\alpha}^n_{i,j-1/2} = 0 \tag{19}$$

is enforced and the method becomes fully first order in a local region. In our experience, this fail-safe mechanism is critical for the success of the FCT algorithm. It should also be noted that after setting $\boldsymbol{\alpha}^n_{i\pm1/2,j\pm1/2} = 0$ in one cell, the problem (negative density etc.) may then appear in a neighbouring cell. In principle the result could be a cascade across all cells. These cascades are rare and do not occur for any of the simulations presented in this work.

This completes the description of the FCT algorithm itself but there is another aspect which must be addressed. In [27] it is recognized that some amount of higher order dissipation must be included to remove high frequency noise generated by the FCT procedure. In that work the high-order dissipation was added to the AD flux prior to flux correction. In our studies we found this to be unsatisfactory because the effect of the high-order dissipation is reduced by the FCT limiters. The result is unacceptable levels of numerical noise in the computed solutions. Therefore we add dissipation independently after the FCT step. To this end we implement a second-order dissipation near shocks [13,16] to treat undamped transverse instabilities as well as a fourth-order Jameson style dissipation away from shocks [31,32,25]. We switch the fourth order dissipation on or off based on density variations to ensure that it is not active near shocks or contacts. One final note is that the computed solution will not violate the prescribed bounds only for CFL numbers less than 1/2 and so all FCT simulation results presented in this paper set the CFL number to be 0.4.

3.3 Sonic fix

As is the case for some other methods, such as Godunov's method with an approximate Roe Riemann solver [14], the FCT method can exhibit poor behavior in rarefaction waves at points where the flow speed is equal to the sound speed (sonic points). The problem is illustrated by the solution to a modified version of Sod's shock tube problem [33,14] with left and right states given by $(\rho, u_1, u_2, p)_L = (1.0, 0.75, 0.0, 1.0)$ and

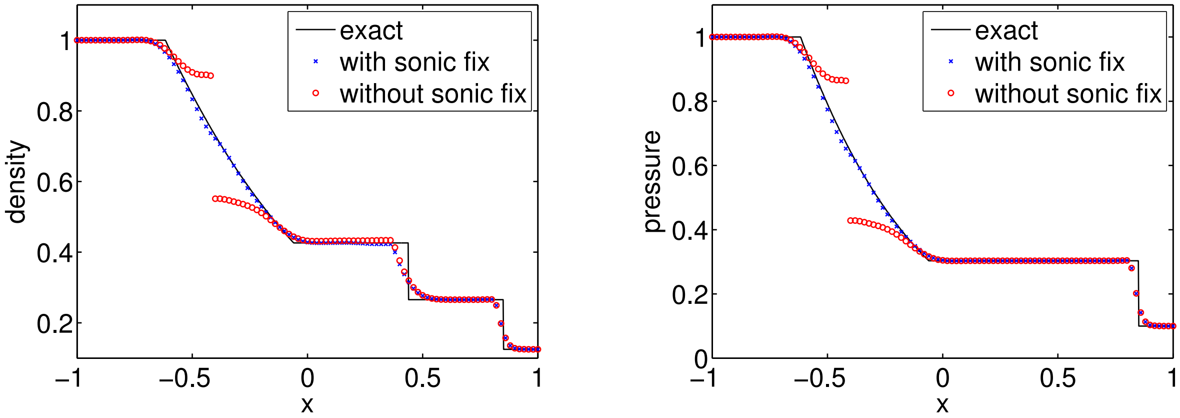

Fig. 1. FCT solution for a shock tube problem containing a sonic rarefaction with and without a sonic fix at $t = 0.5$. The black line represents the exact solution, the red circles the numerical approximation without the sonic fix and the blue crosses the numerical approximation with the sonic fix. The problematic behavior at the sonic point is quite clear in both the density (left) and pressure (right).

$(\rho, u_1, u_2, p)_R = (0.125, 0.75, 0.0, 0.1)$, and with $\gamma = 1.4$. We compute approximations to the solution of this Riemann problem using the grid $\mathcal{L}([-1,1], 100)$ where

$$\mathcal{L}([x_a, x_b], N) = \left\{ x_i \mid x_i = x_a + i\Delta x,\ \Delta x = (x_b - x_a)/N, i = 0, 1, \dots, N \right\}, \tag{20}$$

with the initial discontinuity located at $x = -0.4$. Figure 1 shows the results produced by the FCT method with and without our sonic fix. The problematic behavior of the method at the sonic point is clearly visible in the form of a rarefaction shock which represents an entropy violating weak solution.

The existence of rarefaction shocks in numerical approximations is typically the result of insufficient numerical diffusion. For FCT this is caused by the use of high-order centered fluxes. This is in contrast to Roe's method where the linearization causes the problem even at first order. The FCT method considered in this paper uses the HLL flux (known to be devoid of rarefaction shocks [14]) for the low order update. To eliminate rarefaction shocks for FCT approximations, we rely on this fact and simply set the value for $\boldsymbol{\alpha}$ in (8) to zero for cases where sonic rarefactions are present. This choice has implications on solution accuracy, but because sonic points exist in isolation, the impact is negligible as will be demonstrated in Section 4.

The anti-diffusive fluxes in (8) have associated left and right states, call these $\mathbf{u}_L$ and $\mathbf{u}_R$ respectively. For instance consider $\mathbf{F1}^{\mathrm{AD},n}_{i+1/2,j}$ with $\mathbf{u}_L = \mathbf{u}^{\mathrm{td},n}_{i,j}$ and $\mathbf{u}_R = \mathbf{u}^{\mathrm{td},n}_{i+1,j}$. These states can be viewed as left and right states of a one dimensional Riemann problem in the direction normal to the cell face. Define the normal velocities as $v_{n,L} = (n_1, n_2) \cdot (u_{1L}, u_{2L})^T$ and $v_{n,R} = (n_1, n_2) \cdot (u_{1R}, u_{2R})^T$ where (n_1, n_2) is the unit normal to the cell face. Following the nomenclature in [14], we define the star state as the center solution to this Riemann problem (i.e. the solution between the $\mathcal{C}^+$ and $\mathcal{C}^-$ characteristics). As in [14], p^* and v_n^* can be approximated by

$$p^* = \left[\max\left(0, \left(c_L + c_R - \frac{\gamma - 1}{2}\left(v_{n,R} - v_{n,L}\right)\right)\left(\frac{c_L}{p_L^z} + \frac{c_R}{p_R^z}\right)^{-1}\right)\right]^{1/z} \tag{21}$$

and

$$v_n^* = v_{n,L} + \frac{2}{\gamma - 1}\left(c_L - c_L^*\right) \tag{22}$$

where $c_L^* = c_L(p^*/p_L)^z$, $c_R^* = c_R(p^*/p_R)^z$, $z = (\gamma - 1)/(2\gamma)$, c_L is the left sound speed, and c_R is the right sound speed. These particular star states arise from the approximation of the Riemann solution by the so-called two

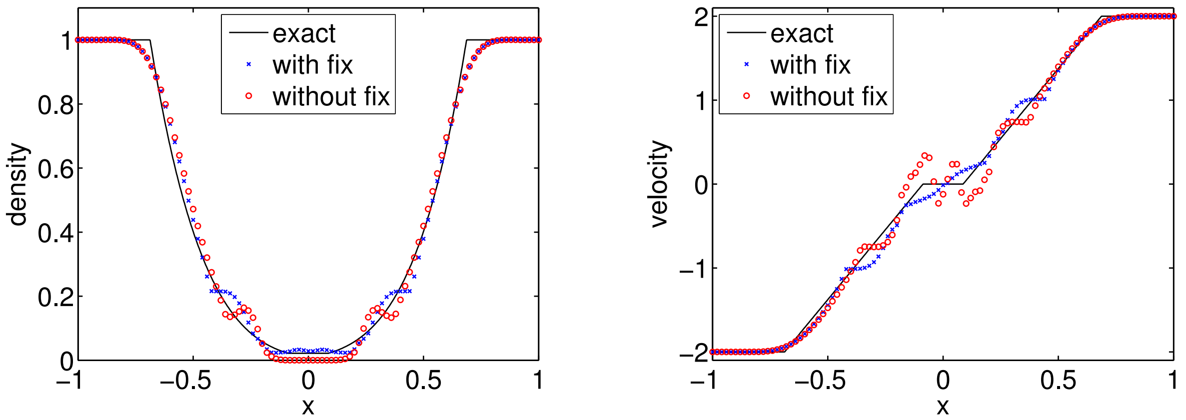

Fig. 2. Density (left) and velocity (right) for a strong rarefaction problem at $t = 0.25$. The black line represents the exact solution, the red circles the FCT approximation without a fix and the blue crosses the FCT solution with the fix. The oscillations in velocity for the original FCT scheme are particularly troubling but also note the undershoot of the density near the origin.

rarefaction Riemann solver and are approximations to the true star state. Note that other choices for the star states are also acceptable. Our sonic fix defines a new value for $\boldsymbol{\alpha}$ by

$$\boldsymbol{\alpha}^n_{i+1/2,j} \leftarrow \begin{cases} 0 & \text{if} \quad v_{n,L} - c_L \le 0 \quad \text{and} \quad v_n^* - c_L^* \ge 0 \\ 0 & \text{if} \quad v_n^* + c_R^* \le 0 \quad \text{and} \quad v_{n,R} + c_R \ge 0 \\ \boldsymbol{\alpha}^n_{i+1/2,j} & \text{else.} \end{cases}$$

The effect of these choices is to return the solver to first order accuracy near sonic points in rarefaction waves. Figure 1 shows the solution to the modified Sod's problem employing this sonic fix where it is seen that the poor behavior has been effectively eliminated apart from a small kink at the sonic point. It should be noted that the particular sonic fix demonstrated here relies on an approximate solution to the Riemann problem. For cases where this solution is not known, this fix is not applicable and sonic rarefactions must be identified in another way. For example, one might consider applying the fix wherever the flow transitions from super- to sub-sonic flow across a cell boundary.

3.4 Strong Rarefactions

In addition to the poor behavior for sonic rarefaction waves, the traditional FCT algorithm runs into difficulties for strong rarefaction waves where the difference in velocities at which the gas is being pulled apart differ by more than the local sound speed. This is a very difficult problem for many methods because a near vacuum state is reached and failure can occur as a result of negative densities or pressures [5]. Consider the solution to a Riemann problem with left and right states $(\rho, u_1, u_2, p)_L = (1.0, -2.0, 0.0, 0.4)$ and $(\rho, u_1, u_2, p)_L = (1.0, 2.0, 0.0, 0.4)$ respectively.

Figure 2 shows the density and velocity as computed by the FCT algorithm for this case both with and without our fix. The FCT solution without any fix demonstrates oscillations in velocity close to the near vacuum state (near the origin). In order to remove this behavior a simple fix is employed which sets

$$\boldsymbol{\alpha}^n_{i+1/2,j} = 0 \quad \text{if} \quad p^* < \min(p_L, p_R) \quad \text{and} \quad |v_{n_L} - v_{n_R}| \ge \max(c_l, c_r).$$

This causes the first order scheme to be used when strong rarefaction waves are present. The results shown in figure 2 demonstrate that the velocity from the fixed scheme is monotonic near the origin. These results are comparable to the results of Tóth in [5] but further improvements should be investigated.

3.5 A Note Concerning Monotonicity

The original FCT scheme of Boris and Book applied to 1-D linear advection problems is provably monotone. However, the extension by Zalesak to higher-dimensions do not result in a monotone scheme, a fact that has apparently not been discussed in the literature. We now present a simple example to illustrate this fact. Consider linear advection with unit advection velocity,

$$\frac{\partial}{\partial t}\rho + \frac{\partial}{\partial x_1}\rho = 0.$$

We use the low-order flux given by $\mathbf{f}^{\text{low},n}_{i+1/2} = \rho^n_i$, and the second-order centered flux given by $\mathbf{f}^{\text{high},n}_{i+1/2} = \frac{1}{2}(\rho^n_i + \rho^n_{i+1})$. At time level t^n let the approximate solution be given by

$$\rho^n_{-3} = 4.5, \quad \rho^n_{-2} = 4, \quad \rho^n_{-1} = 3.5, \quad \rho^n_0 = 3, \quad \rho^n_1 = 3, \quad \rho^n_2 = 2, \quad \rho^n_3 = 1, \quad \rho^n_4 = 0.$$

Set the grid spacing as $\Delta x_1 = 1$ and the temporal spacing as $\Delta t = 0.25$. The FCT algorithm, as outlined by Zalesak [27,28], produces the following values for $\boldsymbol{\alpha}$

$$\boldsymbol{\alpha}^n_{-1/2} = 1, \quad \boldsymbol{\alpha}^n_{1/2} = 1, \quad \boldsymbol{\alpha}^n_{3/2} = 1.$$

By using the forward Euler time integrator (i.e. $\rho^{n+1}_i = \rho^{\text{new}}_i$), the FCT solution after a single step results in the values

$$\rho^{n+1}_0 = 3.0625, \quad \rho^{n+1}_1 = 3.125.$$

The solution at time t^n was monotonically decreasing left to right while the solution for these two cells at time t^{n+1} is monotonically increasing left to right and so the violation of monotonicity is demonstrated. Many authors suggest the use of a pre-limiter, but for this case the pre-limiter suggested by Zalesak [27] and Kuzmin [6] has no effect as can be easily verified. The pre-limiter of DeVore [4], which we have adopted here, does remedy this particular problem, but a proof of monotonicity for arbitrary high order fluxes is not known.

4 Numerical Results

We now present simulation results using the FCT algorithm described in Section 3. The discussion centers on studying the robustness and accuracy of the overall numerical approach and comparing the results to those from the high-resolution Godunov method in [16–18] which uses an approximate Roe Riemann solver [34] and the MinMod limiter [14]. Of course, the comparisons presented here are only valid for these particular implementations of the FCT and Godnuov methods. There are many variations to both algorithms which would change the specifics of the results. However, the present study provides a reasonable baseline comparison of the relative merits of the two schemes. Furthermore, the hope is that given the results from previous comparisons, for example in [22], one can place, in a general sense, high-resolution Godunov methods, WENO methods, and FCT in relation to each other. In fact the tests we present were largely driven by the choice of tests presented in [22] exactly for the reason that comparisons could be made.

Because the purpose of this section is to provide a comparison between methods as they might be used in practice, the set of parameters used by each method is set to what we consider to be reasonable numbers. For the Godunov method we use CFL= 0.9 and for FCT we use CFL= 0.4. The small choice for FCT is required, as noted in Section 3, to ensure the desired bounds are not violated. For problems where AMR is used, the refinement criteria is the same for both schemes and is based on a weighted sum of first and second un-divided differences of the solution (see [16] for details).

The expected second-order convergence rate for the FCT method for smooth flows has been established using the method of analytic solutions [35]. This test was also performed for the Godunov method as in [18]. Here we consider the solution to 1-D isolated contacts, isolated shocks, Sod's shock tube problem, a two-shock Riemann problem, and the Shu-Osher test case. The methods are then compared for the 2-D problems of shock impingement on a cylinder and the irregular Mach reflection of a strong shock on an inclined ramp.

4.1 Isolated Contact and Shock Discontinuities

4.1.1 Contact wave

The contact wave is a traveling discontinuous jump where characteristics run parallel to the front. As such, error can accumulate with the result that a nominally P^{th} order shock capturing scheme will generally converge at the rate of $\kappa = P/(P+1)$ in the L_1 sense [36–38]. There are some so-called compressively limited schemes which can achieve $\kappa = 1$ convergence although such schemes often have other undesirable characteristics such as the artificial steepening of smooth solutions [39,14]. The construction of the FCT method does not immediately indicate what the convergence rate should be.

The initial conditions for the contact wave consists of the left state $(\rho, u_1, u_2, p)_L = (0.1, 1.0, 0.0, 1.0)$ and the right state $(\rho, u_1, u_2, p)_R = (1.0, 1.0, 0.0, 1.0)$ with the jump at $x_0 = 0.25$. We can construct a weak solution corresponding to a vanishing viscosity solution, and we will call such solutions "exact" with the understanding that there may be many weak solutions. The exact solution to this problem consists of a propagating discontinuity moving to the right with speed 1.0. The density jumps through this discontinuity but the pressure and velocity remain constant. Simulations are performed on the grid defined by $\mathcal{L}([0.0, 1.0], 200m)$ where m is a measure of grid resolution (see equation(20)). A value of $\gamma = 1.4$, corresponding to a diatomic ideal gas, is chosen.

A convergence study is performed at various numerical resolutions indicated by m with the comparisons taking place at $t_f = 0.5$ using the discrete L_1 norm. Results from this study are given in Table 1 where the convergence rate is computed from one resolution to the next as $\kappa = \log_2(e_\rho(m)/e_\rho(2m))$ as well as a least squares fit of the rates over the entire refinement process which we label $\tilde{\kappa}$. Here it is seen that both the FCT

m	$e_\rho(m)$ F	κ	$e_\rho(m)$ G	κ
1	1.06e−2	–	1.39e−2	–
2	6.64e−3	.67	8.78e−3	.66
4	4.18e−3	.67	5.55e−3	.66
8	2.63e−3	.67	3.51e−3	.66
$\tilde{\kappa}$	.67		.66	

Table 1
Convergence results for the contact wave problem using second order Godunov and FCT approximations, indicated by "F" and "G" in the headings respectively. L_1 errors in density at $t_f = 0.5$ are computed for grid resolutions determined by m. Estimated convergence rates $\kappa = \log_2(e_\rho(m)/e_\rho(2m))$ as well as a least squares fit of the convergence rates over the entire refinement process $\tilde{\kappa}$ are shown. Note that errors for velocity and pressure are identically zero.

and Godunov methods attain the expected convergence rate of $\approx 2/3$ as measured by both κ and $\tilde{\kappa}$. We can also see that the FCT method captures the contact with slightly less error than the Godunov method although the results for the Godunov method are sensitive to the choice of Riemann solver and limiter [38].

4.1.2 Shock wave

Consider a Mach 2 shock with $\gamma = 1.4$. The pre- and post-shock states are given by $(\rho, u_1, u_2, p)_L = (2.67, 1.48, 0.0, 4.5)$ and $(\rho, u_1, u_2, p)_R = (1.0, 0.0, 0.0, 1.0)$. For this nonlinear phenomenon, the characteristic curves enter into the discontinuity which acts as a natural steepening mechanism. Computations are carried out on the unit interval $x \in [0, 1]$ using mesh $\mathcal{L}([0.0, 1.0], 200m)$ with m being a measure of grid resolution. The initial jump is placed at $x_0 = 0.25$ and integration is carried out to $t_f = 0.25$ where L_1 errors are computed. The results are presented in Table 2.

m	$e_\rho(m)$ F	κ	$e_\rho(m)$ G	κ	$e_{u_1}(m)$ F	κ	$e_{u_1}(m)$ G	κ	$e_p(m)$ F	κ	$e_p(m)$ G	κ
1	8.38e−3	–	7.08e−3	–	5.59e−3	–	4.83e−3	–	1.44e−2	–	1.26e−2	–
2	3.94e−3	1.0	3.65e−3	.96	2.91e−3	.94	2.76e−3	.81	6.57e−3	1.1	6.35e−3	.99
4	2.08e−3	.92	1.82e−3	1.0	1.39e−3	1.1	1.22e−3	1.2	3.63e−3	.86	3.27e−3	.96
8	9.63e−4	1.1	9.15e−4	.99	7.13e−4	.96	6.72e−4	.86	1.66e−3	1.1	1.60e−3	1.0
$\tilde{\kappa}$	1.03		.99		1.00		.97		1.02		.99	

Table 2
Convergence results for the shock wave problem using second order Godunov (G) and FCT (F) approximations. L_1 errors in density, velocity and pressure are shown at $t_f = 0.25$ for grid resolutions determined by m. Estimated convergence rates $\kappa = \log_2(e_\rho(m)/e_\rho(2m))$ as well as a least squares fits of the convergence rates over the entire refinement process $\tilde{\kappa}$ are also shown.

Both schemes have similar L_1 errors and demonstrate the expected first order convergence with $\kappa \approx 1$ and $\tilde{\kappa} \approx 1$ for density, velocity and pressure. This implies that the number of cells for which there is $O(1)$ point-wise error is fixed which implies that the shock does not continually smear as a function of time. Contrast this to the case of the contact in Section 4.1.1 where the captured discontinuity contains an increasing number of grid cells even as its overall width decreased.

4.2 Sod's shock tube problem (modified)

For this example problem we investigate the behavior of the FCT and Godunov methods for a modified version of Sod's shock tube problem. This problem is designed to highlight the poor behavior of some numerical methods near sonic points in rarefaction waves and was previously discussed in Section 3.3 where the sonic fix for the FCT method was described. A description of sonic fixes for Godunov schemes can be found, for example, in [14]. The computational domain is again chosen to be $x \in [-1, 1]$, the initial jump is placed at $x_0 = -0.4$, and the governing equations (1) are integrated to $t_f = 0.5$. The computational grid for this study is given by $\mathcal{L}([-1.0, 1.0], 100m)$.

The exact density and pressure, as well as approximate results for $m = 1$ for both the Godunov and FCT methods, are shown in Figure 3 which demonstrates the similarity of the two approximate solutions. This trend continues for all resolutions but is more easily seen for this coarse simulation where $m = 1$. Figure 3 also shows that both methods seem to be handling the sonic rarefaction. Quantitative convergence results are shown in Table 3 using the discrete L_1 norm. These results indicate that although both schemes are clearly converging

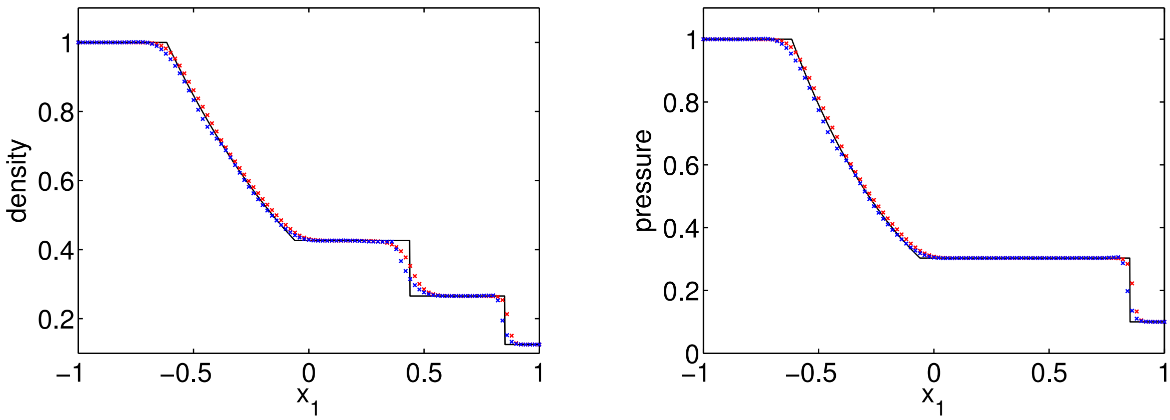

Fig. 3. Exact solution (black line) and numerical approximations with $m = 1$ for Godunov's method using Roe's approximate Riemann solver (red marks) and the FCT method (blue marks) for the modified Sod shock tube problem at $t_f = 0.5$. Shown here are the density (left) and the pressure (right).

m	$e_\rho(m)$ F	κ	$e_\rho(m)$ G	κ	$e_{u_1}(m)$ F	κ	$e_{u_1}(m)$ G	κ	$e_p(m)$ F	κ	$e_p(m)$ G	κ
2	8.86e−3	–	9.44e−3	–	1.44e−2	–	1.44e−2	–	6.54e−3	–	6.32e−3	–
4	5.00e−3	.83	5.31e−3	.83	6.99e−3	1.0	7.51e−3	.94	3.21e−3	1.0	3.22e−3	.97
8	3.05e−3	.71	3.03e−3	.81	3.32e−3	1.1	4.08e−3	.88	1.54e−3	1.1	1.67e−3	.94
16	1.83e−3	.74	1.80e−3	.75	1.59e−3	1.1	2.42e−3	.75	7.24e−4	1.1	9.08e−4	.88
$\tilde{\kappa}$	.76		.80		1.06		.86		1.06		.93	

Table 3

Convergence results for the modified Sod shock tube problem. Discrete L_1 error and associated convergence rates for the Godunov (G) and FCT (F) schemes at selected resolutions associated with the choice of m. Apparently the mesh is of insufficient resolution for the methods to exhibit global convergence rates of $2/3$ for the L_1 norm of density which is dictated by the captured contact.

to the exact solution, neither scheme is yet in the asymptotic range of convergence where the L_1 error of density will be dominated by the $2/3$ convergence rate near the contact. Even so, both schemes provide similar convergence behavior with the FCT yielding slightly higher convergence rates for the pressure and velocity.

4.3 A Two-Shock Riemann Problem

The last Riemann problem investigated in this work is commonly known as the two-shock problem. The exact solution to this problem for $\gamma = 1.4$ has a $M \approx 5.62$ shock in the rightmost characteristic field, a $M \approx 1.81$ shock in the leftmost characteristic field, and a contact wave separating the two. Left and right states are taken from [14] and given as $(\rho, u_1, u_2, p)_L = (5.99242, 19.5975, 0.0, 460.894)$ and $(\rho, u_1, u_2, p)_R = (5.99242, -6.19633, 0.0, 46.0950)$ The exact solution is determined as in [30], and results in a nearly stationary shock for the leftmost characteristic field. The actual speed of the left shock is $S \approx 0.78$, the velocity through the contact wave is $u_1 \approx 8.69$, and the rightmost shock moves with speed $S \approx 12.25$. The capturing of the nearly stationary shock proves to be one of the primary difficulties for this problem (see [40,41] for details on slowly moving shocks). Shock capturing schemes also have difficulty representing the contact in this problem and there is a need to accurately resolve that jump before a reasonable global approximation is achieved.

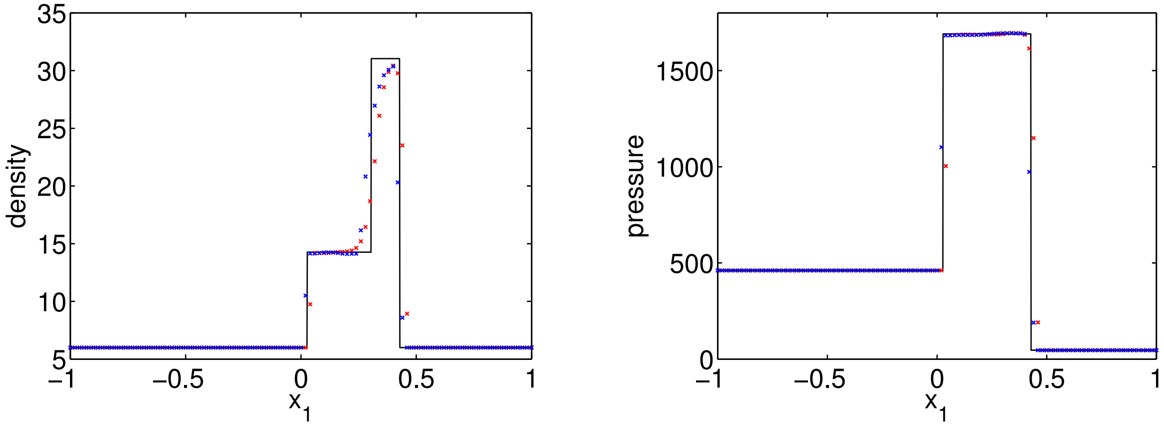

Fig. 4. Exact solution (black line) and approximations with $m = 1$ for Godunov's method using Roe approximate Riemann solver (red marks) and the FCT method (blue marks) for the two-shock Riemann problem at $t_f = 0.035$. Shown here are the density (left) and the pressure (left).

The solution for this problem is approximated for $x \in [-1, 1]$ using the mesh $\mathcal{L}([-1.0, 1.0], 100m)$ and integration is carried out to a final time of $t_f = 0.035$. Figure 3 shows profiles of density and pressure for the exact solution at that time as well as the numerical approximations for $m = 1$. Qualitatively it is seen that the two schemes produce similar results, however, close inspection revels the Godunov approximation to be slightly less oscillatory particularly in the pressure while the FCT approximation shows a sharper capture of the contact wave. Table 4 shows quantitative convergence results for the two schemes using the discrete L_1 norm for the computation of the errors. This table shows that the Godunov approximations demonstrate somewhat higher convergence rates for all quantities, but that for the resolutions discussed here the FCT approximations always give smaller actual errors. In fact for the pressure and velocity, the errors in the FCT approximations are more than three times smaller than the Godunov approximations at coarse resolutions and still more than twice as small for the finest mesh considered.

m	$e_\rho(m)$ F	κ	$e_\rho(m)$ G	κ	$e_{u_1}(m)$ F	κ	$e_{u_1}(m)$ G	κ	$e_p(m)$ F	κ	$e_p(m)$ G	κ
2	4.48e−1	–	7.53e−1	–	1.10e−1	–	3.40e−1	–	8.74e0	–	3.29e1	–
4	2.58e−1	.80	4.08e−1	.88	7.15e−2	.62	1.41e−1	1.3	6.49e0	.43	1.40e1	1.23
8	1.51e−1	.77	2.26e−1	.85	2.48e−2	1.5	7.78e−2	.86	3.34e0	.96	7.89e0	.83
16	9.00e−2	.75	1.43e−1	.66	1.66e−2	.58	4.76e−2	.71	1.82e0	.88	4.94e0	.66
$\tilde{\kappa}$	.77		.80		.91		.94		.75		.90	

Table 4
Discrete L_1 error and associated convergence rates for the two shock problem using the Godunov (G) and FCT (F) schemes at selected resolutions associated with the choice of m. Neither scheme is yet in the asymptotic range of convergence where the L_1 errors in density will be dominated by the 2/3 convergence rate at the contact.

4.4 Shu-Osher Problem

The final one-dimensional test case considered in this paper is a problem originally considered by Shu and Osher [7] and subsequently by others [22,23]. This problem consists of a $M = 3$ shock in air, $\gamma = 1.4$, traveling into unshocked air with sinusoidally perturbed density. As originally presented, the problem has a number of parameters and the specific values used here are taken from [22]. The initial setup is

$$\begin{aligned} &\rho = 3.857143, && u_1 = 2.629369,\ u_2 = 0,\ p = 10.33333 && \text{for } x_1 < -4 \\ &\rho = 1 - \epsilon \sin(\lambda \pi x),\ && u_1 = 0, \qquad\quad\ \ u_2 = 0,\ p = 1 && \text{for } x_1 \geq -4 \end{aligned} \tag{23}$$

where the parameter values are $\epsilon = 0.2$ and $\lambda = 5$. The approximate solution is computed for $x \in [-5, 5]$ using $\mathcal{L}([-5.0, 5.0], 200m)$ and integrated to a final time $t_f = 1.8$.

When interpreting results, it is useful to understand the Riemann structure of the solution when $\epsilon = 0$. For this case we can determine an exact solution and the waves present there give a good indication where structures in the more complicated solution will arise. When $\epsilon = 0$, the solution consists of a $M = 3$ shock traveling with speed $S \approx 3.55$. The perturbed problem, $\epsilon \neq 0$ and small, will have disturbances traveling along the other two characteristic fields with speeds $S \approx 2.63$ and $S \approx 0.69$. At $t = 1.8$, the lead shock will have travelled to $x_1 \approx 2.39$, the contact wave to $x_1 \approx 0.73$ and the left acoustic wave to $x_1 \approx -2.76$. For small ϵ it is expected that the exact solution will change character near these locations.

A reference solution, computed with $m = 128$ up to $t = 1.8$, can be seen, for example, in Figure 5. For $x < -2.76$ the solution is the unperturbed post-shock state. For $x \in (-2.76, 0.73)$ the solution exhibits mild oscillations in all quantities. These oscillations are the result of the passage of the left acoustic wave. For $x \in (0.73, 2.39)$ the solution exhibits high frequency oscillations. Notice that for the computational resolution m, the high frequency oscillations in the density for $x \in (0.73, 2.39)$ contain approximately $2m$ grid points per wavelength. The solution with $m = 128$ uses a sufficiently fine grid to resolve these oscillations as evidenced by the fact that further refinement does not change the character of the solution, and because it results in approximately 256 cells per wavelength for $x \in (0.73, 2.39)$. For $x > 2.39$ the solution returns to the initial upstream state. The locations where the solution changes behavior are, as expected, those mentioned above in the discussion of the Riemann structure for $\epsilon = 0$.

There is no known closed form solution to this problem and convergence results must be estimated through comparison to more finely resolved solutions. Here we use a method similar to that presented in [42]. At a given point, x_i, we assume the solution at a given resolution differs from the exact solution by

$$\mathbf{u}_e(x_i) - \mathbf{u}_m(x_i) \approx \mathbf{c}(x_i) h_m^\kappa \tag{24}$$

where $\mathbf{u}_e$ is the exact solution, $\mathbf{u}_m$ the numerical approximation, $\mathbf{c}(x_i)$ depends only on x_i, κ is the convergence rate and h_m is the grid spacing. Note that we have uniform grid spacing. From (24) one can compute

$$||\mathbf{u}_{m_1}(x) - \mathbf{u}_{m_2}(x)||_h \approx ||\mathbf{c}(x)||_h \left| h_{m_1}^\kappa - h_{m_2}^\kappa \right| \tag{25}$$

using a discrete norm. Numerical approximations at three resolutions and equation (25) can be combined to produce two equations which define the convergence rate κ and the constant $||\mathbf{c}(x)||_h$. The solution error can then be approximated as $e_\mathbf{u}(m) = ||\mathbf{u}_e - \mathbf{u}_m||_h \approx ||\mathbf{c}(x)||_h h^\kappa$. When estimating the error and convergence rate for a given approximation with resolution given by m, we use the three approximations $\mathbf{u}_m$, $\mathbf{u}_{64}$ and $\mathbf{u}_{128}$. Table 5 shows the convergence results using the discrete L_1 norm for both the FCT and Godunov schemes. From this table it is clear that the coarser resolutions do not approximate the solution well at all, particularly for the density, and low rates of convergence are attained. Figures 5 and 6 demonstrate this graphically where the numerical approximations for $m = 1$ are plotted on top of the reference solution. Figure 5 shows the

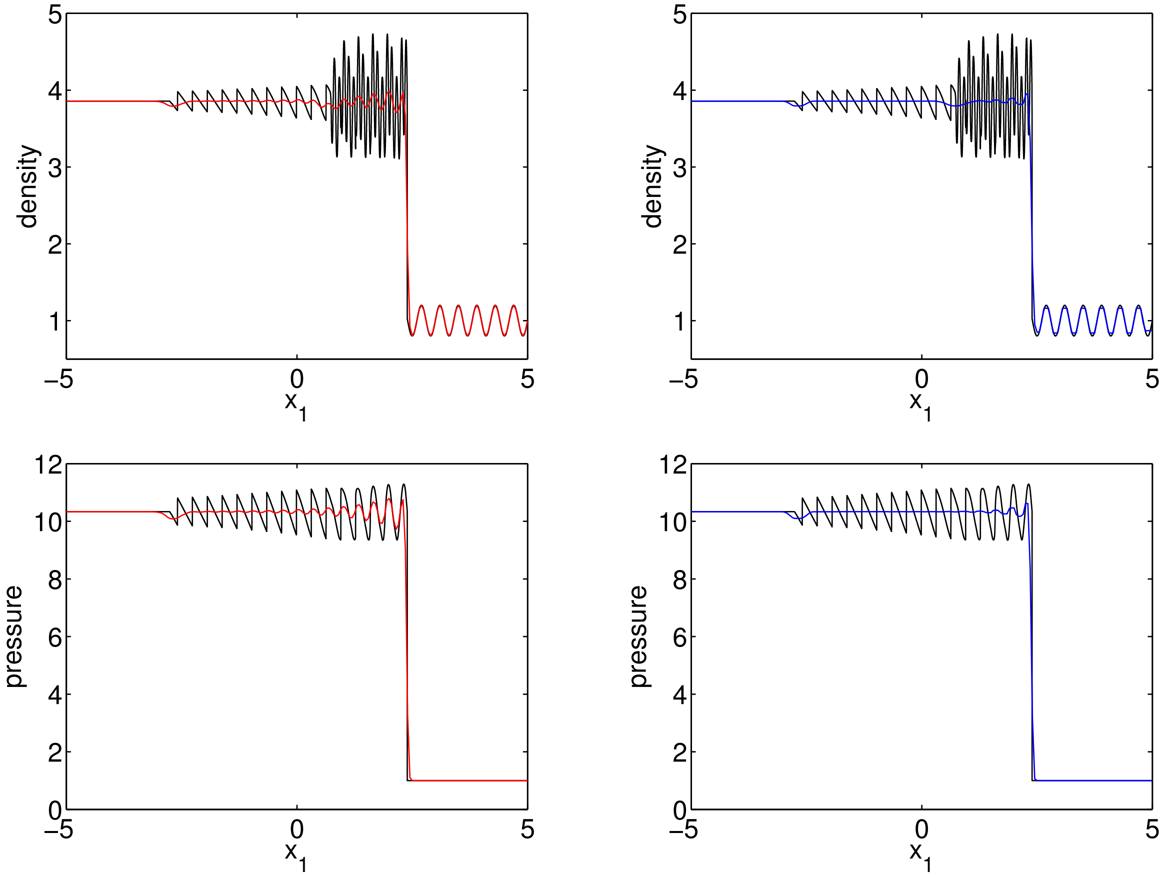

Fig. 5. Comparison of the numerical approximations with $m = 1$ at $t = 1.8$ for the Shu-Osher test problem. For all images the black line represents the reference solution with $m = 128$ while the red line (left) shows the Godunov approximation and the blue line (right) shows the FCT approximation. From top to bottom are density and pressure.

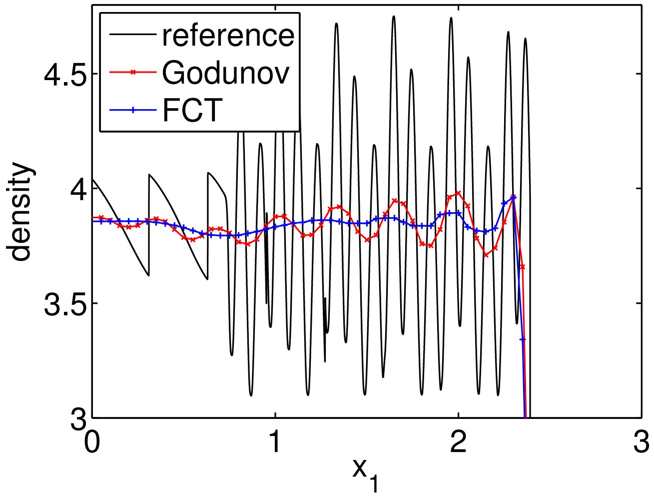

Fig. 6. Zoom of density near the high frequency oscillations. Shown are the FCT and Godunov approximations wtih $m = 1$, and the reference solution computed by the Godunov method with $m = 128$.

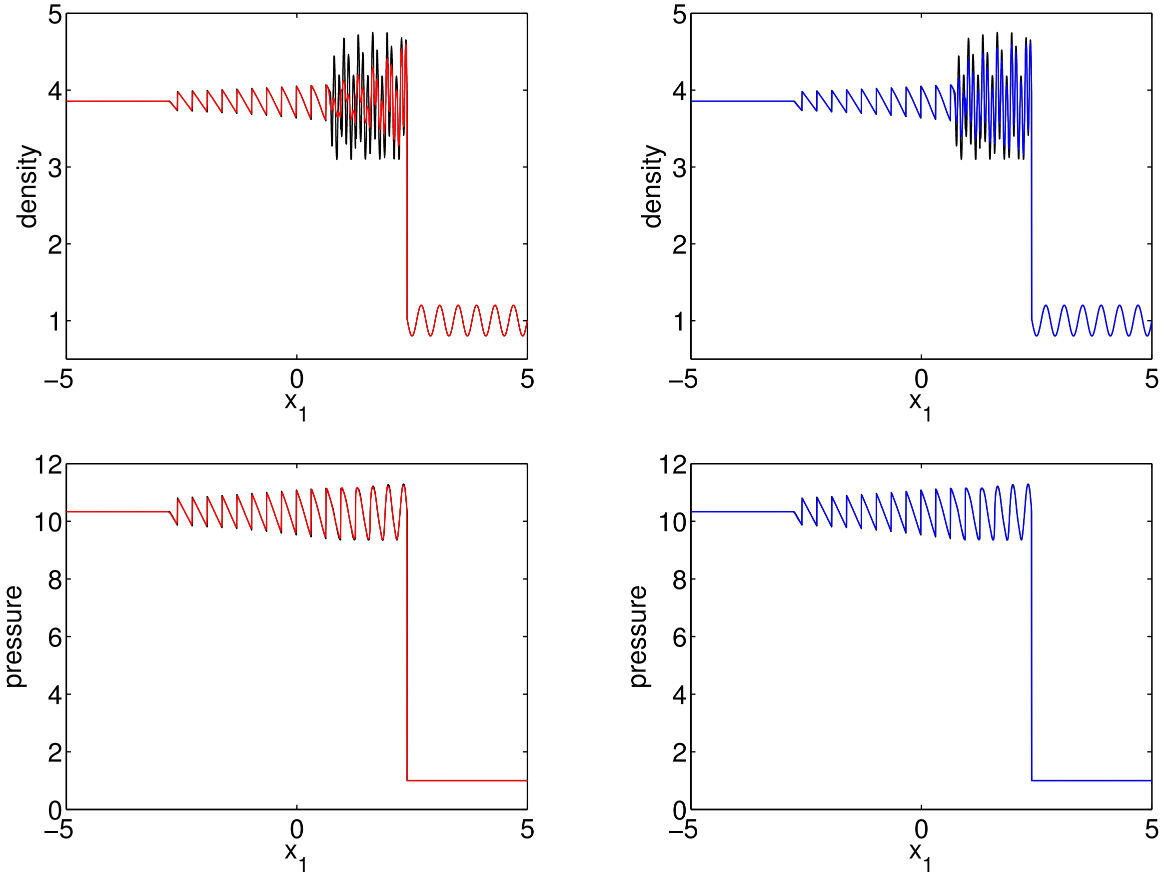

Fig. 7. Comparison of the numerical approximations at $t = 1.8$ for the Shu-Osher test problem and $m = 16$. For all images the black line represents the reference solution with $m = 128$ while the red line (left) shows the Godunov approximation and the blue line (right) shows the FCT approximation. From top to bottom are density and pressure.

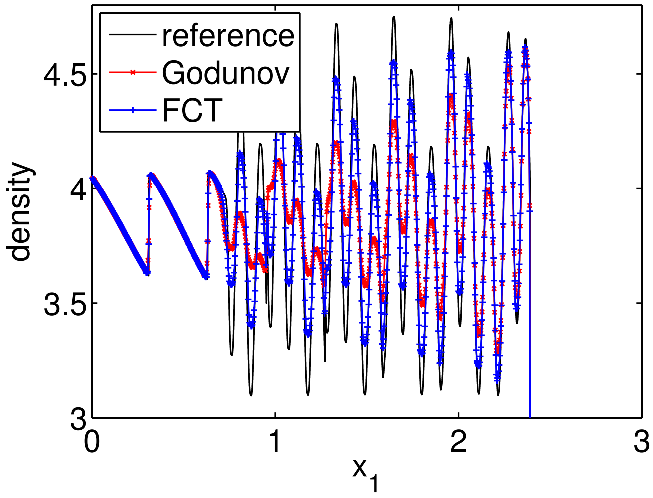

Fig. 8. Zoom of density near the high frequency oscillations. Shown are the FCT and Godunov approximations wtih $m = 16$, and the reference solution computed by the Godunov method with $m = 128$.

m	$e_\rho(m)$ F	κ	$e_\rho(m)$ G	κ	$e_{u_1}(m)$ F	κ	$e_{u_1}(m)$ G	κ	$e_p(m)$ F	κ	$e_p(m)$ G	κ
1	1.16e0	.75	1.20e0	.44	3.44e−1	1.1	3.02e−1	.94	2.34e0	1.1	1.98e0	.92
2	9.18e−1	.86	1.01e0	.52	1.57e−1	1.1	1.55e−1	.94	1.08e0	1.1	1.08e0	.93
4	7.86e−1	1.1	8.64e−1	.67	6.35e−2	1.1	7.85e−2	.92	4.75e−1	1.1	5.67e−1	.94
8	5.98e−1	1.4	7.28e−1	.93	3.10e−2	1.1	4.22e−2	.94	2.23e−1	1.1	2.94e−1	.93
16	2.39e−1	1.4	5.00e−1	1.3	1.52e−2	1.2	2.35e−2	1.0	1.06e−1	1.2	1.70e−1	1.1
32	8.90e−2	1.4	2.19e−1	1.5	6.87e−3	1.4	1.20e−2	1.3	4.57e−2	1.3	8.38e−2	1.3

Table 5
Convergence results for the Shu-Osher test problem using both the Godunov (G) and FCT (F) methods. Convergence rates and errors are computed with (24) and (25) using finely resolved simulations at $m = 64$ and $m = 128$.

global character of the solution and Figure 6 shows a zoom of the density in the most oscillatory region. For low resolutions, the high frequency oscillations are not well represented and both methods exhibit poor convergence properties, particularly for the density as seen in Figure 6. This is reflected by the convergence rates which are less than 1. At some critical resolution however, both methods see a rise in convergence rates, tending to some value larger than 1. Once this transition occurs, the high frequency oscillations begin to be well represented as shown in Figures 7 and 8. This transition to higher convergence rates happens at lower resolution for FCT, indicating that it has more resolving power than the Godunov method. For the highest resolutions demonstrated here, both approximations are reasonably representing all structures in the flow and their convergence rates become roughly equal. However, because the FCT method experienced the transition to higher convergence rates earlier in the refinement process, the errors at the highest resolutions are smaller than for the Godunov approximations by nearly a factor of 2.

4.5 Shock Impingement on Stationary Cylinder

The first two-dimensional test problem which we consider is the impingement of a $M = 2$ shock on a rigid immovable cylinder. The basic problem consists of a rigid cylinder of radius 0.5 placed in the larger domain $[-2, 2] \times [-2, 2]$. A Mach 2 shock initially located at $x_1 = -1.5$ runs from left to right. The computational mesh is defined as the overlapping grid constructed from an annulus $\mathcal{A}((0, 0), [0.5, 1.0], 10m, 80m)$ and a rectangle $\mathcal{R}([-2, 2] \times [-2, 2], 80m, 80m)$, where $\mathcal{A}$ and $\mathcal{R}$ are defined as

$$\mathcal{R}([x_{1,a}, x_{1,b}] \times [x_{2,a}, x_{2,b}], N_1, N_2) = \big\{(x_{1,a} + i_1\Delta x_1\, ,\ x_{2,a} + i_2\Delta x_2) \mid$$
$$\Delta x_k = (x_{k,b} - x_{k,a})/N_k,\ i_k = 0, 1, \ldots, N_k,\ k = 1, 2\big\}$$

and

$$\mathcal{A}\left((x_{1,c}, x_{2,c}), [r_a, r_b], N_r, N_\theta\right) = \big\{(x_{1,c}, x_{2,c}) + r_{i_r}(\cos(\theta_{i_\theta}), \sin(\theta_{i_\theta})) \mid$$
$$r_{i_r} = r_a + i_r(r_b - r_a)/N_r,\ \theta_{i_\theta} = 2\pi i_\theta/N_\theta,\ i_k = 0, 1, \ldots, N_k,\ k = r, \theta\big\}.$$

The boundary around the cylinder is defined as a slip wall (see [17]), the left boundary as an inflow, and the remaining boundaries are given outflow conditions. Phenomena of interest are limited to those associated with the shock/cylinder interaction. Provided that the simulation is not run too far in time, waves generated at the cylinder do not reach the exterior boundaries and so the exterior boundary condition choice has little influence.

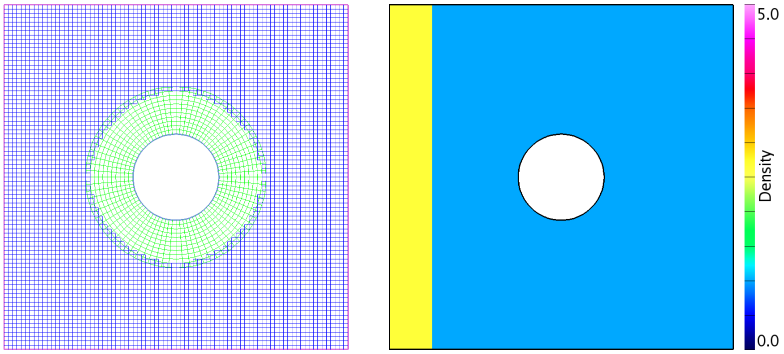

Fig. 9. Overlapping grid structure (left) and color contour of the initial density (right). The overlapping grid structure is used to capture geometry and additional adaptive grids will be dynamically added to locally increase resolution. Note that we only require one layer of interpolation points at grid overlap as discussed in Section 3.1. The initial density shows a $M = 2.0$ shock in air (ideal gas with $\gamma = 1.4$) moving from left to right.

Figure 9 shows the computational mesh as well as color contours of density for the initial conditions. Numerical values for the initial conditions in primitive quantities, corresponding to a Mach 2 shock in air ($\gamma = 1.4$), were shown previously in Section 4.1.2.

The comparisons carried out in this paper use the resolution $m = 1$ displayed in Figure 9 for the coarse grid simulation. Adaptive mesh refinement (AMR) is then used for successive resolutions. For this test of shock interaction with a single cylinder, additional levels of AMR use a factor four refinement in each coordinate direction and so the four resolutions investigated have approximate grid spacings $h \approx 0.05$, 0.0125, 0.003125, and 0.00078125. Notice that because the initial condition uses a perfect jump, there exists numerical artifacts along the c^- characteristic and contact path. No effort is made to remove these and their contribution may be seen throughout the simulations.

Figure 10 shows the computed density using both methods for $t = 0.6$, $t = 1.0$, and $t = 1.4$ as the incident shock reflects from the cylinder boundary. Overall the results show remarkably good agreement although slight differences can be seen at $t = 1.4$ in the low density wake region of the cylinder. To give a better indication of what is happening, Figure 11 shows the AMR grid structure, numerical Schlieren images [43], and the estimated error in density at $t = 1.4$. The computation of the error estimate will be discussed below. The image of the AMR grids is perhaps the most informative because it demonstrates the increased noise created by the FCT method. Numerical noise tends to flag cells for refinement by the AMR algorithm and so a larger portion of the domain is covered by fine meshes for the FCT simulation. This type of noise, also interpretable as staircases [6], is a common phenomenon in FCT simulations. There are ways to reduce the noise, such as adding higher levels of artificial diffusion, using different high order fluxes, and others, but in our experience, there is no single method which completely eliminates it. On the other hand the results from the Godunov method show little sign of this phenomenon and the AMR meshes conform closely to the locations of rapid change, such as shocks and contacts. The plots of estimated error also show increased noise in the FCT solution. It is worth noting that the remnant of the initial condition on the c^- characteristic has flagged refinement for the FCT solution whereas this feature has been smoothed by the Godunov method.

Figure 12 shows line plots of the approximations along the lines $x_2 = 0$ with $x_1 \in [0.5, 2.0]$ and $x_1 = 1$ with $x_2 \in [0, 2]$ which gives an indication of convergence as the mesh is refined. From these plots one can again see the trend that FCT approximations contain more noise as compared to the Godunov approximations which generally vary more smoothly. Table 6 shows estimated L_1-norm self convergence errors and convergence rates. These errors and rates were computed using the finest three resolutions following the approach presented in [42] and as outlined in Section 4.4. An advantage to this method is that it naturally provides an estimate for the exact solution $\mathbf{u}_e$ in equation (24). This result can be used to estimate solution errors as was done to obtain

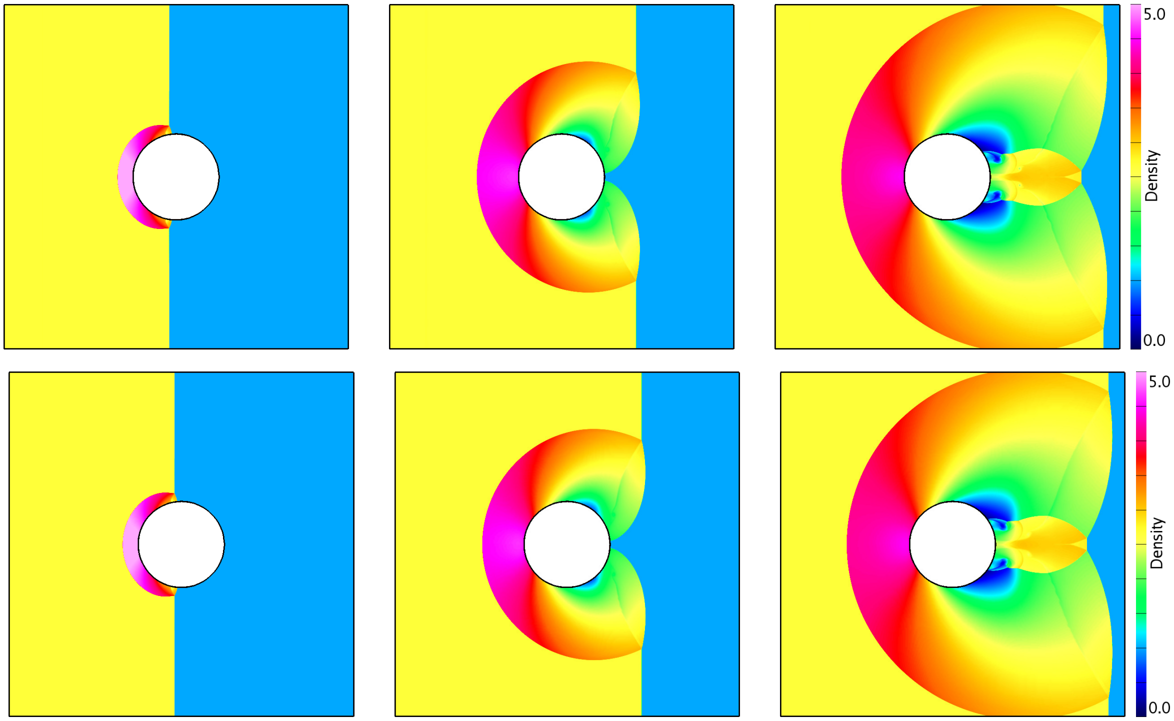

Fig. 10. Color contours of density for the finest resolution using FCT (top) and Godunov's method (bottom) at $t = 0.6$ (left), $t = 1.0$ (middle), and $t = 1.4$ (right).

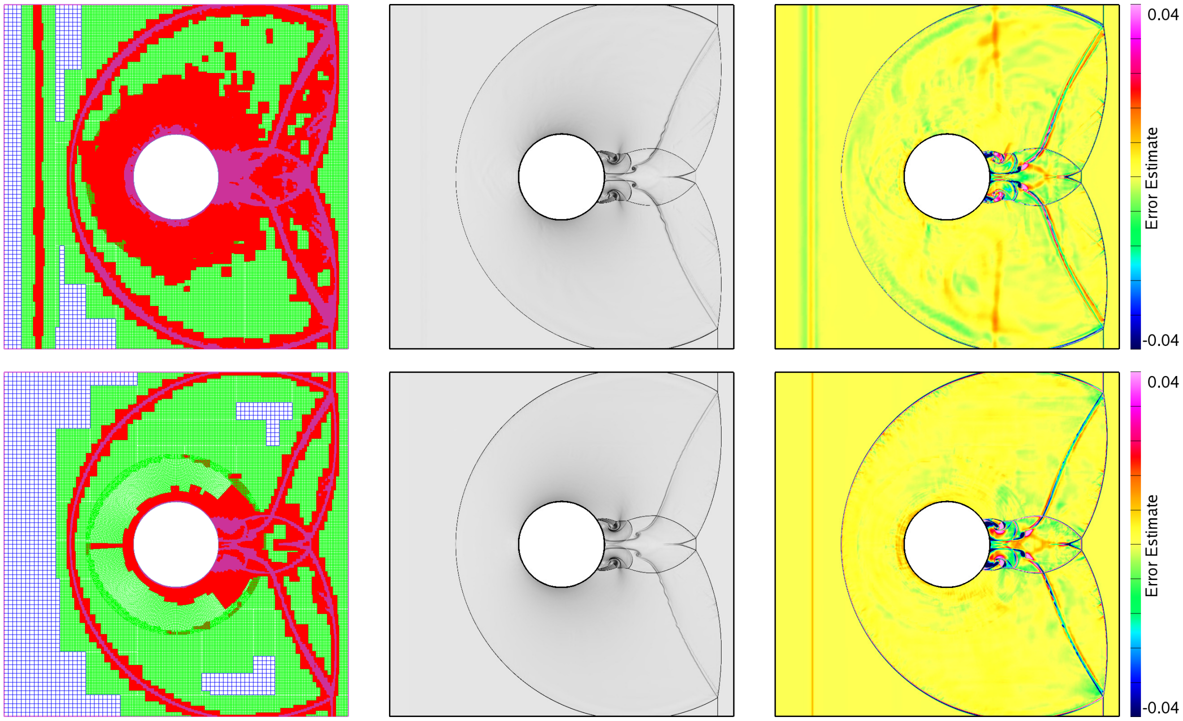

Fig. 11. AMR grid structure (left), numerical Schlieren images (center) and estimated L_1-error in density (right) for the FCT method (top) and Godunov's method (bottom) for the finest resolution simulation at $t = 1.4$.

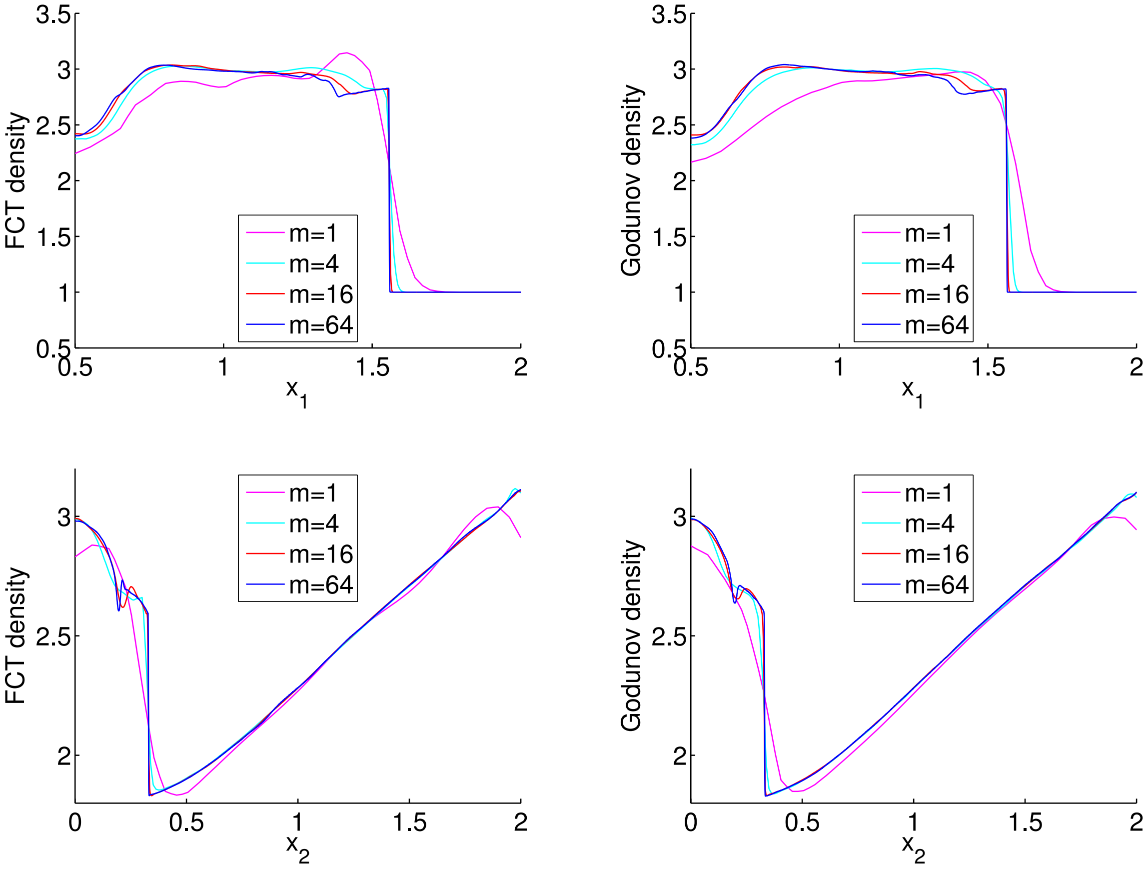

Fig. 12. Solution convergence along the lines $x_2 = 0$ (top) and $x_1 = 1$ (bottom) for the FCT method (left) and the Godunov method (right) on the shock-cylinder problem. Shown here is the density with the colors indicating numerical resolution. Maroon represents the solution with no AMR while cyan, red, and finally blue represent 1, 2, and 3 levels of additional factor four adaptive meshes respectively.

the error estimates shown in Figure 11. The results in Table 6 show that the errors and convergence rates are

m	$e_\rho(m)$ F	$e_\rho(m)$ G	$e_{u_1}(m)$ F	$e_{u_1}(m)$ G	$e_{u_2}(m)$ F	$e_{u_2}(m)$ G	$e_p(m)$ F	$e_p(m)$ G
4	1.54e−2	1.91e−2	1.02e−2	1.32e−2	7.55e−3	8.77e−3	3.00e−2	3.75e−2
16	5.60e−3	7.49e−3	3.70e−3	5.76e−3	3.13e−3	3.00e−3	1.06e−2	1.45e−2
64	2.03e−3	2.94e−3	1.35e−3	2.52e−3	1.29e−3	1.03e−3	3.73e−3	5.60e−3
κ	0.73	0.67	0.73	0.60	0.64	0.77	0.75	0.69

Table 6
Computed errors and convergence rates for the FCT (F) and Godunov (G) schemes on the problem of shock-cylinder interaction. Here we use a weighted L_1-norm.

similar for the FCT and Godunov methods. It is interesting to see that convergence results for all quantities, including the velocities and pressure which do not jump through contact waves, show sub-linear convergence. The probable cause for this behavior is the complex interactions of shocks, contacts and rarefactions as well as the instabilities in the wake region of the flow. Indications of this are given by the error estimates of Figure 11

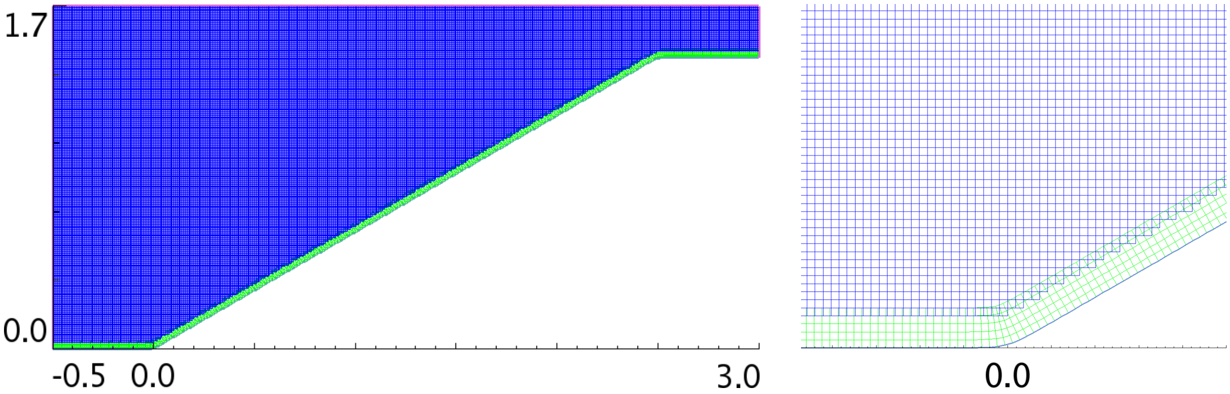

Fig. 13. Basic overlapping grid used for the simulation of irregular Mach reflection on an inclined ramp. The boundary fitted ramp grid is seen in green and the background Cartesian mesh in blue. The full geometry (left) shows what looks like sharp transitions to represent the ramp corners, but the zoom near the origin (right) shows that these corners are very slightly rounded.

where the wake region is shown to have large errors over a substantial area.

4.6 Irregular Mach Reflection of a Strong Shock

The final test considered in this paper is that of irregular Mach reflection of a strong shock at an inclined ramp. This classic example has been investigated by many authors [28,44,23] as well as demonstrated experimentally [45]. In this problem, a Mach 10 shock impacts a ramp which is inclined 30° from the normal shock propagation direction. The result is a complex interaction and results in an irregular Mach reflection. Numerically, this flow can cause a carbuncle like instability [46,47] for some numerical methods if proper care is not taken.

Traditionally this test problem has been solved by inclining the incident shock to a Cartesian grid and using special boundary conditions to simulate the transition region at the start of the ramp. For the simulations presented in this paper, the geometry of a 30° ramp is realized using overlapping grids and then a Mach 10 shock is impacted onto this ramp. The overlapping grid we use consists of a thin boundary fitted mesh to model the ramp in union with a background Cartesian mesh for the remaining bulk of the computational domain. The background Cartesian mesh is defined by the rectangle $\mathcal{R}([-0.5, 3.0] \times [0, 1.7], 420, 340)$. Although the boundary fitted mesh is not described by a simple mathematical expression, a verbal description will suffice for our purpposes. The physical boundary of this ramp grid is defined as a curve that smoothly transitions from the line $x_2 = 0$, to the line $x_2 = x_1/\sqrt{3}$, and finally to the line $x_2 = 1.4438$. These transitions are defined in terms of integrals of hyperbolic tangent functions and are therefore smooth [48]. The ramp grid is extruded along normals into the domain and the mesh spacing is chosen to approximately match that of the background Cartesian grid. The resulting overlapping grid is shown in Figure 13 where both the full geometry and a zoom near the ramp initiation at the origin are shown. At the scale of the full geometry it is difficult to see the rounding of the corners, but the close up image makes this rounding clear. A rounded corner will have some effect on the solution as it compares to a solution obtained using a perfectly sharp corner. Such effects have been studied for example in [49,16] and found to be of little consequence when the radius of curvature is small as compared to the flow features of interest (as is the case here).

Initial conditions for a Mach-10 planar shock in air ($\gamma = 1.4$) are $(\rho, u_1, u_2, p)_L = (8.0, 8.25, 0.0, 116.5)$ and $(\rho, u_1, u_2, p)_R = (1.4, 0.0, 0.0, 1.0)$. The initial shock is located at $x_1 = -0.25$ (for reference the left-most boundary is $x_1 = -0.5$ and the ramp incline begins at $x_1 = 0$) and time integration is performed to $t = 0.2$. Boundary conditions are set using a slip wall condition along the ramp boundary, inflow conditions along the left boundary and outflow conditions elsewhere. For these simulations, the base mesh has roughly equal mesh

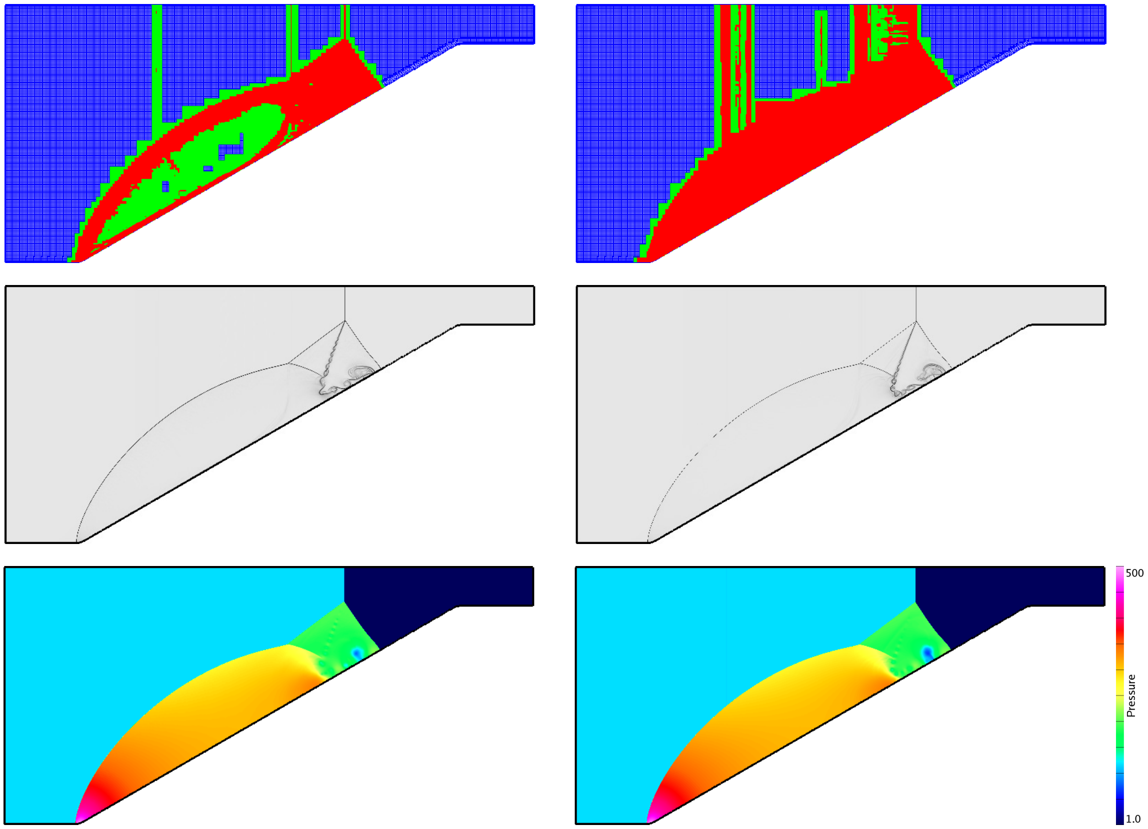

Fig. 14. Simulation results at $t = 0.2$ for the Godunov method (left) and FCT (right) with 3 levels of factor 4 refinement. Shown are the AMR mesh (top), a numerical Schlieren image (middle), and pressure (bottom). Notice the increase in noise produced by the FCT method as evidenced by the larger region flagged for AMR refinement. Also notice the lower pressure achieved by the FCT method within the main vortex.

spacing throughout the domain with $h \approx \frac{1}{120}$. Simulations are performed at four resolutions starting with only the base mesh and then progressing through to use one additional level of factor four refinement, two additional levels of factor three refinement, and finally two additional levels of factor four refinement.

Figure 14 shows the approximations obtained using the FCT and Godunov methods at the finest resolution with approximate mesh spacing $h \approx 5.21 \times 10^{-4}$. At this scale there are some apparent differences that merit mention. First notice the increased noise production by the FCT method as shown by the increased proportion of the domain flagged for AMR refinement. Also both simulations retain remnants of the initial condition along the c^- characteristic and contact path. These remnants are covered with fine AMR meshes, although the refinement for the FCT algorithm covers a larger region. Finally it is seen that the minimum pressure inside the main vortex is lower for the FCT simulation than for Godunov.

Figure 15 shows close-up numerical Schlieren images near the main vortex structure at the four different mesh resolutions. For both simulation techniques, the main vortex is poorly represented at low resolutions but with increasing mesh resolution the main features begin to develop. The roll-ups along the slip lines become pronounced for both methods with the Godunov solution showing slightly more detailed structure. The final two solutions show interesting differences in the development of the main vortex. For the Godunov method it remains as a coherent single vortical structure, while for the FCT method it begins to break down and show more complex behavior. Comparing this behavior with what is seen in [23] shows that the Godunov methods (for [23] the PPM method) tend to maintain a coherent single structure, while the other methods (the hybrid WENO method in [23] and FCT here) produce a vortex which begins to loose coherence at very high resolution.

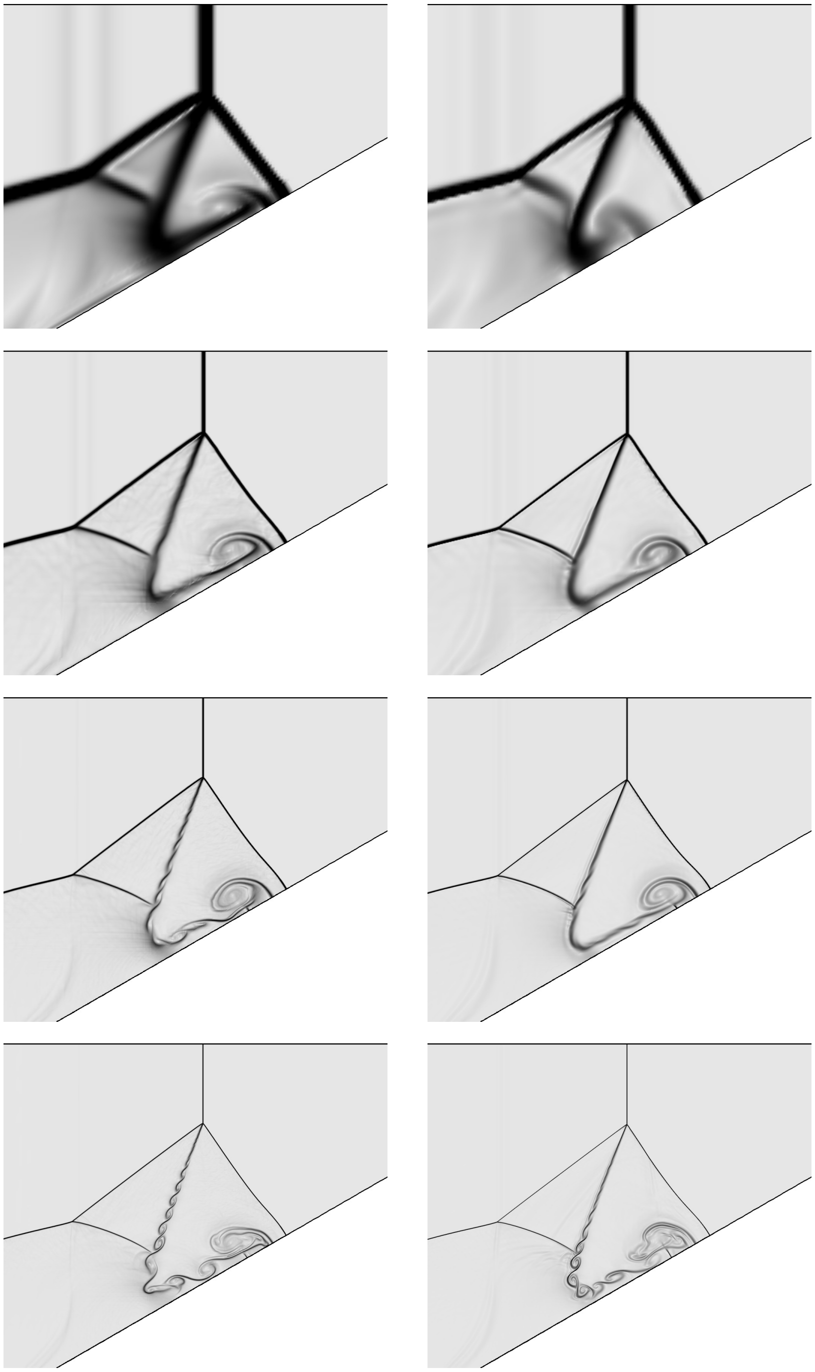

Fig. 15. Zoom of the numerical Schlieren images near the triple point and main vortex for Godunov (left) and FCT (right). Resolution increases from top to bottom with approximate grid spacings $h \approx 1/120$, $1/480$, $1/1080$, and $1/1920$ respectively.

This type of behavior calls into question the limit processes of the various schemes and whether the various methods are in fact approaching the same vanishing viscosity solution. This is an interesting question and will be the subject of future work. As a further comparison of the methods, Figure 16 compares the peak vorticity and minimum scaled temperature, defined as p/ρ, for the two methods as a function of grid resolution. For both schemes the minimum temperature decreases and the maximum vorticity increases as the mesh is refined.

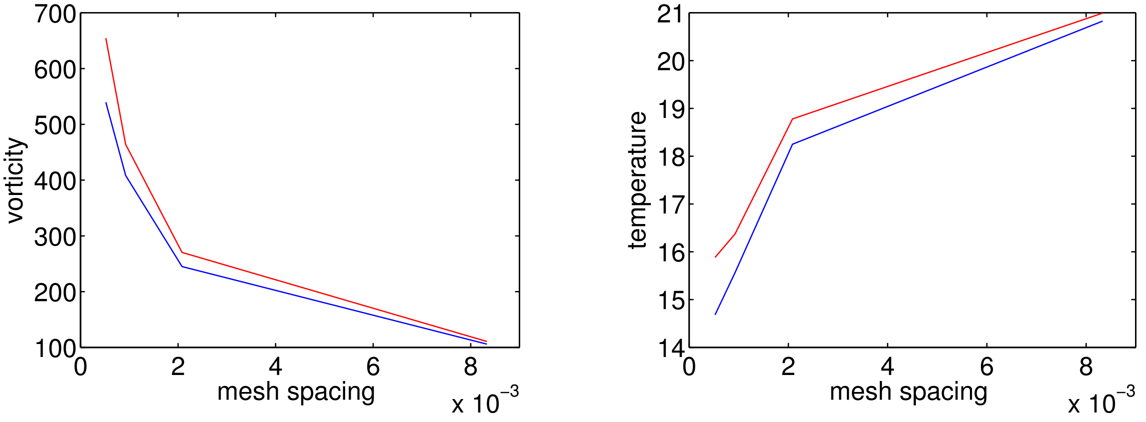

Fig. 16. Maximum vorticity within the main vortex as a function of mesh spacing (left) and minimum scaled temperature (right), defined as p/ρ, as a function of mesh spacing. Godunov results are given in red and FCT results in blue.

The FCT results show a lower temperature and smaller vorticity as compared to the Godunov results. A self convergence study is performed as was done in Section 4.5 using a weighted L_1-norm. The finest three resolutions are used for this comparison and results presented in Table 7. Here it is seen that the performance of the two methods is similar. The L_1-norm convergence rates are somewhat low but this is attributed to the large variations in the solution and unstable vortical flows which arise at the slip line which is evident in Figure 15.

m	$e_\rho(m)$ F	$e_\rho(m)$G	$e_{u_1}(m)$ F	$e_{u_1}(m)$ G	$e_{u_2}(m)$ F	$e_{u_2}(m)$ G	$e_p(m)$ F	$e_p(m)$ G
4	5.67e−2	6.29e−2	3.15e−2	3.45e−2	3.32e−2	3.89e−2	1.06e0	1.09e0
9	3.71e−2	4.25e−2	1.74e−2	2.32e−2	2.05e−2	2.84e−2	6.85e−1	6.81e−1
16	2.75e−2	3.22e−2	1.14e−2	1.76e−1	1.46e−2	2.28e−2	5.04e−1	4.87e−1
κ	0.52	0.48	0.73	0.49	0.59	.39	0.54	0.58

Table 7
Computed errors and convergence rates for the FCT (F) and Godunov (G) schemes on the problem of irregular Mach reflection. Here we use a weighted L_1 norm.

5 Qualitative Comments About Timings

As previously mentioned, one aim of this study is to provide a reasonably detailed comparison of an FCT method with a high-resolution Godunov method. In this assessment, a quantitative comparison of these techniques has included convergence results as well as details concerning the relative accuracy of the methods on a set of test problems. One critical aspect that has been neglected until this point is a discussion of the computational expense. This question has not been addressed for the very specific reason that the Godunov code used here is mature and has been through years of optimization. The FCT code however, has been recently developed for the purposes of this study and has not been through the same optimization process. However, we do believe that some qualitative remarks about issues related to efficiency are in order.

As implemented, the FCT method is approximately 10 times slower per time step than the Godunov method. Some part of this comes from a non-optimal implementation, but a much larger part is due to the FCT algorithm being more costly than the Godunov method. One major factor is that the FCT method requires approximately 60 characteristic transformations per cell per time step (see for example equation (10)) compared to only about 8 for the Godunov method. Computational expense is also increased by the larger number of refinement grids that result from the high-frequency noise present in FCT solutions. For example, the finest FCT resolution of irregular Mach reflection in Section 4.6 has 1.8 times as many grid cells as the Godunov method at the final time. Assuming the majority of the cells reside on the finest level of refinement, a relatively accurate assumption here, this results in roughly 1.8 times the computational cost. Furthermore, the FCT method generally runs at a lower CFL number than the Godunov method due to the monotonicity limit and the additional stability constraint from the fourth-order dissipation. Taking the ramp computations as an example, the end result was approximately a factor of 2.8 reduction in time step size for FCT as compared to Godunov. Taken together, this indicates that the FCT method is potentially quite costly when compared to Godunov. For every case presented here, a simulation at substantially higher resolution, and commensurately smaller error, can be obtained by the Godunov method for a given amount of wall clock time. Using the ramp computation again as an example, the finest FCT approximations required roughly 30 times more wall clock time than did the Godunov approximations. This means that for the computational cost of the Godunov simulation with $m = 16$, the FCT method could only be run with $m \approx 5$ (see Table 7 and Figure 15). However, as noted earlier, in the case where no Riemann based strategies are viable (such as for a lack of knowledge of the detailed eigen-structure of the system or for possible robustness reasons) an FCT approach can provide a viable path forward. In such cases, it is irrelevant how much faster other techniques might have been because they are not available or not practical.

6 Conclusions

This paper has outlined the development and assessment of a high-resolution FCT algorithm for the Euler equations on structured overlapping grids. The implementation of the FCT method for overlapping grids was based on the Overture framework and included modifications and extensions to the classical FCT algorithm. These extensions included the modifications required for the discretization on curvilinear grids as well as the inclusion of a Jameson-style fourth-order artificial viscosity to remove the high frequency noise produced by FCT. Improvements were made to the FCT algorithm to eliminate entropy violating shocks that can occur at sonic points in rarefaction waves. Difficulties occurring in strong rarefaction waves, where a near vacuum state is produced when the gas separates at velocities greater than the sound speed, were also addressed.

We have evaluated this new FCT method on a series of benchmark high-speed flow problems and compared the results to those obtained using a high-resolution Godunov method. This investigation confirmed the expected convergence character for isolated contact and shock waves. In two dimensions, the overlapping grid capabilities were used to study the refraction of a planar shock with a rigid cylinder and irregular Mach reflection of a strong shock on an inclined ramp. For problems with known exact solutions actual errors and estimated convergence rates were determined. For problems with no known solutions, estimated errors and convergence rates were calculated based on a self convergence assumption. Overall the results obtained by the FCT and Godunov methods were found to be very similar. The FCT solutions tended to have a somewhat higher resolving capability but also to contain more numerical noise. It was recognized that our implementation of the FCT method was quite costly in comparison to the Godunov method. This is due to the large number of characteristic transformations, the smaller time step required, and the apparent difficulty in removing high frequency noise which tends to flag cells for refinement by the AMR algorithm. In the end, the comparisons suggest that the FCT method may be a viable option for cases where Riemann solutions are not possible, or for unstructured meshes where a Godunov type method may not be easily implemented.

References

[1] J. P. Boris, D. L. Book, Flux-corrected transport. I. SHASTA, a fluid transport algorithm that works, J. Comput. Phys. 11 (1973) 38–69.

[2] J. P. Boris, D. L. Book, K. Hain, Flux-corrected transport II: Generalizations of the method, J. Comput. Phys. 18 (1975) 248–283.

[3] J. P. Boris, D. L. Book, Flux-corrected transport III. Minimal-error FCT algorithms, J. Comput. Phys. 20 (1976) 397–431.

[4] C. Richard DeVore, Flux-corrected transport techniques for multidimensional compressible magnetohydrodynamics, J. Comput. Phys. 92 (1991) 142–160.

[5] G. Tóth, D. Odstrcil, Comparison of some flux corrected transport and total variation diminishing numerical schemes for hydrodynamic and magnetohydrodynamic problems, J. Comput. Phys. 128 (1) (1996) 82–100.

[6] D. Kuzmin, R. Löhner, S. Turek (Eds.), Flux-Corrected Transport, Springer, 2005.

[7] G.-S. Jiang, C.-W. Shu, Efficient implementation of weighted eno schemes, J. Comput. Phys. 126 (1) (1996) 202–228.

[8] D. S. Balsara, C.-W. Shu, Monotonicity preserving weighted essentially non-oscillatory schemes with increasingly high order of accuracy, J. Comput. Phys. 160 (2) (2000) 405–452.

[9] A. Harten, B. Engquist, S. Osher, S. Chakravarthy, Uniformly high order accurate essentially non-oscillitory schemes, III, J. Comput. Phys. 71 (1987) 231–303.

[10] C.-W. Shu, S. Osher, Efficient implementation of essentially non-oscillatory shock-capturing schemes, J. Comput. Phys. 77 (2) (1988) 439–471.

[11] C.-W. Shu, S. Osher, Efficient implementation of essentially non-oscillatory shock-capturing schemes, II, J. Comput. Phys. 83 (1) (1989) 32–78.

[12] A. Harten, P. D. Lax, B. van Leer, On upstream differencing and Godunov type schemes for hyperbolic conservation laws, SIAM Rev. 25 (1983) 33–61.

[13] P. Colella, P. R. Woodward, The piecewise parabolic method (PPM) for gas-dynamical simulations, J. Comput. Phys. 54 (1) (1984) 174–201.

[14] E. F. Toro, Riemann Solvers and Numerical Methods for Fluid Dynamics, Springer, Berlin, 1999.

[15] G. Chesshire, W. Henshaw, Composite overlapping meshes for the solution of partial differential equations, J. Comput. Phys. 90 (1990) 1–64.

[16] W. D. Henshaw, D. W. Schwendeman, An adaptive numerical scheme for high-speed reactive flow on overlapping grids, J. Comput. Phys. 191 (2) (2003) 420–447.

[17] W. D. Henshaw, D. W. Schwendeman, Moving overlapping grids with adaptive mesh refinement for high-speed flow, J. Comput. Phys. 216 (2) (2006) 744–779.

[18] J. W. Banks, D. W. Schwendeman, A. K. Kapila, W. D. Henshaw, A high-resolution Godunov method for compressible multi-material flow on overlapping grids, J. Comput. Phys. 223 (2007) 262–297.

[19] T. Baker, Mesh generation for the computation of flowfields over complex aerodynamic shapes, Computers Math. Applic. 24 (1992) 103–127.

[20] W. Chan, A unified overset grid generation graphical interface and new concepts on automatic gridding around surface discontinuities, in: Proceedings of the 4th Symposium on Overset Composite Grid and Solution Technology, 1998.

[21] N. A. Petersson, Hole-cutting for three-dimensional overlapping grids, SIAM J. Sci. Comp. 21 (1999) 646–665.

[22] J. A. Greenough, W. J. Rider, A quantitative comparison of numerical methods for the compressible euler equations: fifth-order WENO and piecewise-linear godunov, J. Comput. Phys. 196 (2004) 259–281.

[23] W. J. Rider, J. A. Greenough, J. R. Kamm, Accurate monotonicity- and extrema-preserving methods through adaptive nonlinear hybridizations, J. Comput. Phys. 225 (2007) 1827–1848.

[24] J. W. Banks, J. N. Shadid, An euler system source term that develops prototype Z-pinch implosions intended for the evaluation of shock-hydro methods, Int. J. Numer. Meth. Fl.Accepted.

[25] W. D. Henshaw, OverBlown: A fluid flow solver for overlapping grids, reference guide, Research Report UCRL-MA-134289, Lawrence Livermore National Laboratory (1999).

[26] M. J. Berger, J. Oliger, Adaptive mesh refinemenr for hyperbolic partial differential equations, J. Comput. Phys. 53 (1984) 484–512.

[27] S. T. Zalesak, Fully multidimensional flux-corrected transport algorithms for fluids, J. Comput. Phys. 31 (1979) 335–362.

[28] S. T. Zalesak, The design of flux-corrected transport (FCT) algorithms on structured grids, Ph.D. thesis, George Mason University (2005).

[29] U. M. Ascher, L. R. Petzold, Computer Methods for Ordinary Differential Equations and Differential-Algebraic Equations, SIAM, Philadelphia, 1998.

[30] G. B. Whitham, Linear and Nonlinear Waves, Wiley-Interscience, New York, 1974.

[31] A. Jameson, W. Schmidt, E. Turkel, Numerical solution of the euler equations by finite volume methods using runge-kutta time-stepping schemes, in: AIAA 14th Fluid and Plasma Dynamic Conference, 1981.

[32] A. Jameson, Transonic flow calculations for aircraft, in: Numerical Methods in Fluid Dynamics, vol. 1127 of Lecture Notes in Mathematics, Springer-Verlag, 1983, pp. 156–242.

[33] G. A. Sod, A survey of several finite difference methods for systems of nonlinear hyperbolic conservation laws, J. Comput. Phys. 27 (1) (1978) 1–31.

[34] P. L. Roe, Approximate Riemann solvers, parameter vectors, and difference schemes, J. Comput. Phys. 43 (1981) 357–372.

[35] J. W. Banks, W. D. Henshaw, J. N. Shadid, An FCT method for high-speed flows on structured overlapping meshes part I: Algorithm description, Research Report 2008-0294J, Sandia National Laboratory (2008).

[36] G. W. Hedstrom, The rate of convergence of some difference schemes, J. SIAM Numer. Anal. 5 (2) (1968) 363–406.

[37] A. Harten, The artificial compression method for computation of shocks and contact discontinuities. I. single conservation laws, Commun. Pur. Appl. Math. 30 (5) (1977) 611–638.

[38] J. W. Banks, T. Aslam, W. J. Rider, On sub-linear convergence for linearly degenerate waves in capturing schemes, J. Comput. Phys. 227 (14) (2008) 6985–7002.

[39] R. J. LeVeque, Numerical Methods for Conservation Laws, Birkhauser, Basel, 1992.

[40] S. Karni, S. Čanić, Computations of slowly moving shocks, J. Comput. Phys. 136 (1997) 132–139.

[41] M. Arora, P. L. Roe, On postshock oscillations due to shock capturing schemes in unsteady flows, J. Comput. Phys. 130 (1997) 25–40.

[42] W. D. Henshaw, D. W. Schwendeman, Parallel computation of three-dimensional flows using overlapping grids with adaptive mesh refinement, J. Comput. Phys. 227 (16) (2008) 7469–7502.

[43] J. W. Banks, W. D. Henshaw, D. W. Schwendeman, A. K. Kapila, A study of detonation propagation and diffraction with compliant confinement, Combust. Theory and Modelling 12 (4) (2008) 769–808.

[44] P. Woodward, P. Colella, The numerical simulation of two-dimensional fluid flow with strong shocks, J. Comput. Phys. 54 (1984) 115–173.

[45] M. V. Dyke, An Album of Fluid Motion, The Parabolic Press, Stanford, California, 1982.

[46] J. J. Quirk, A contribution to the great riemann solver debate, Int. J. Numer. Meth. Fl. 18 (1994) 555–574.

[47] M. Dumbser, J.-M. Moschetta, J. Gressier, A matrix stability analysis of the carbuncle phenomenon, J. Comput. Phys. 197 (2004) 647–670.

[48] W. Henshaw, Mappings for Overture, a description of the Mapping class and documentation for many useful Mappings, Research Report UCRL-MA-132239, Lawrence Livermore National Laboratory (1998).

[49] A. K. Kapila, D. W. Schwendeman, J. B. Bdzil, W. D. Henshaw, A study of detonation diffraction in the Ignition-and-Growth model, Combust. Theory and Modelling.